Chemical Engineering Journal 446 (2022) 137243

Contents lists available at ScienceDirect

Chemical Engineering Journal

journal homepage: www.elsevier.com/locate/cej

Tumor site-specific PEG detachment and active tumor homing of therapeutic PEGylated chitosan/folate-decorated polydopamine nanoparticles to augment antitumor efficacy of photothermal/chemo combination therapy

Ming-Hung Hsieh [a], Tzu-Hao Wang [a], Shang-Hsiu Hu [b], Tsai-Ching Hsu [c,e,f], Jia-Le Yow [c], Bor-Show Tzang [c,d,e,f,*], Wen-Hsuan Chiang [a,*]

[a] Department of Chemical Engineering, National Chung Hsing University, Taichung 402, Taiwan
[b] Department of Biomedical Engineering and Environmental Sciences, National Tsing Hua University, Hsinchu 300, Taiwan
[c] Institute of Medicine, Chung Shan Medical University, Taichung 402, Taiwan
[d] Department of Biochemistry, School of Medicine, Chung Shan Medical University, Taichung 402, Taiwan
[e] Immunology Research Center, Chung Shan Medical University, Taichung 402, Taiwan
[f] Clinical Laboratory, Chung Shan Medical University Hospital, Taichung 402, Taiwan

ARTICLE INFO

Keywords:
Tumor-acidity sensitivity
Polydopamine
PEG detachment
Active tumor homing
Benzoic imine bonds
Photothermal/chemo combination therapy

ABSTRACT

To effectively promote tumor-targeted delivery of photothermal/chemo combined therapy for boosted antitumor efficacy, the versatile photothermal hybrid polymeric nanoparticles capable of detaching poly(ethylene glycol) (PEG) segments and exposing tumor-targeting folate (FA) moieties in response to tumor extracellular acidity (pH_e) are developed to selectively deliver doxorubicin (DOX), a chemotherapy drug, to the tumor sites. Through one-pot co-deposition of dopamine molecules with acidity-responsive benzoic imine-containing PEGylated chitosan (BI-PC) adducts, the hybrid BI-PC/polydopamine (PDA) nanoparticles were attained as DOX vehicles and characterized to have a spherical structure composed of a PDA core surrounded by hydrophilic BI-PC shells. The DOX@BI-PC/PDA nanoparticles not only showed prominent colloidal stability in serum-containing environment and photothermal conversion efficiency, but also exhibited acidity/photothermal-activated drug release. The PEG detachment and FA exposure of FA-DOX@BI-PC/PDA nanoparticles in weak acidic environment appreciably promoted their uptake by FA receptor-overexpressed CT-26 colon cancer cells, thus largely augmenting anticancer potency based on the photothermal/chemo therapy. Importantly, the pH_e-responsive FA-DOX@BI-PC/PDA nanoparticles markedly accumulated in CT-26 tumor sites in vivo and inhibited tumor growth without significant systemic toxicity upon the near infrared (NIR)-triggered hyperthermia integrated with DOX chemotherapy. This work presents a practical strategy for improved antitumor potency of photothermal/chemo combination therapy.

1. Introduction.

To enhance anticancer efficacy and diminish adverse effect by effective tumor deposition of chemotherapy agents through the inherent enhanced permeability and retention (EPR) effect of solid tumors, a varied of nanoparticle-based drug delivery systems (DDS) have been created in the past two decades [1–7]. In spite of the rapid progress in development of new DDS for tumor-targeted drug delivery, the increased multidrug resistance and metastasis of cancer cells still largely lower anticancer potency of nanomedicine-enabled chemotherapy [8–10]. To overcome these challenges, several research groups ambitiously combined chemotherapy with different therapeutic modalities (e.g. photothermal therapy (PTT), photodynamic therapy (PDT), chemodynamic therapy (CDT) and immunotherapy) to enhance antitumor efficiency by a synergistic effect [4,11–17]. Due to many advantages of near-infrared (NIR)-mediated PTT including the minimal invasiveness, high tissue penetration, well-controlled spatiotemporal selectivity, oxygen independence and initiation of innate/adaptive immunity by

* Corresponding authors at: Institute of Medicine, Chung Shan Medical University, Taichung 402, Taiwan (B.S. Tzang).
E-mail addresses: bstzang@csmu.edu.tw (B.-S. Tzang), whchiang@dragon.nchu.edu.tw (W.-H. Chiang).

https://doi.org/10.1016/j.cej.2022.137243
Received 28 February 2022; Received in revised form 3 May 2022; Accepted 25 May 2022
Available online 27 May 2022

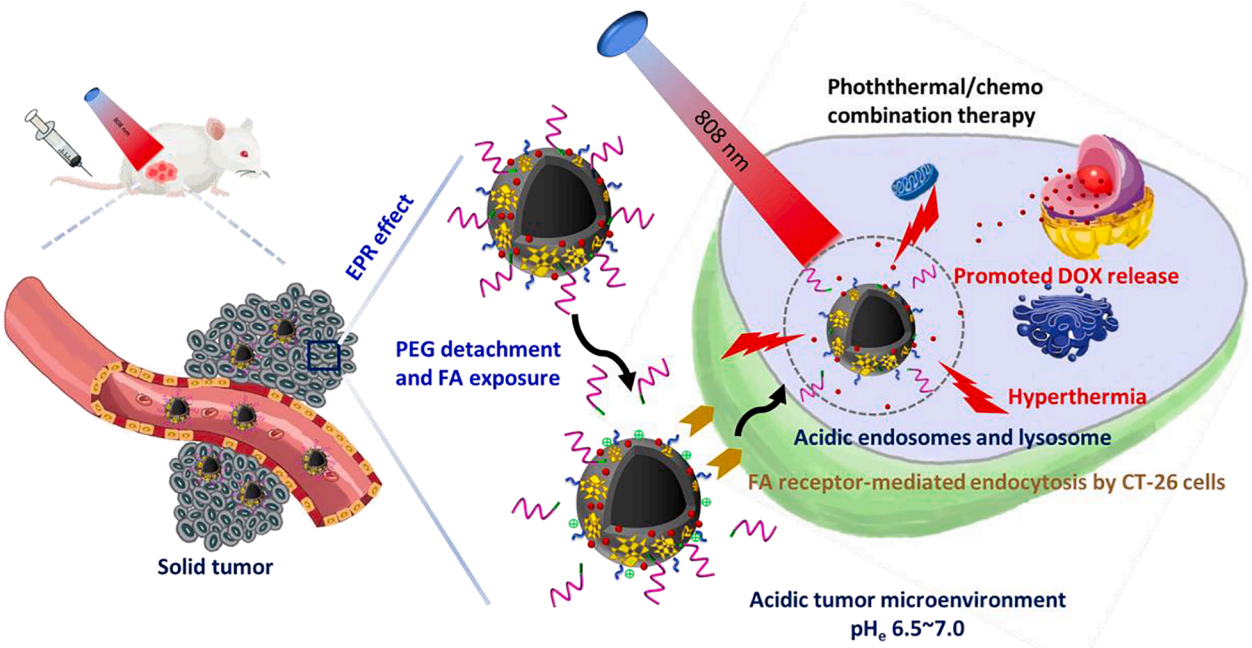

Scheme 1. Illustration of the pH$_e$-triggered dePEGylation and active FA targeting of FA-DOX@BI-PC/PDA nanoparticles to promote their cellular uptake and antitumor efficacy based on photothermal/chemo combinatorial therapy.

antigens released from necrotized cancer cells, the PTT combined with chemotherapy has attracted considerable attention for boosted antitumor efficacy [11–14]. Recently, various NIR-absorbing nanoparticles, including gold nanorods [18], inorganic nanoparticles [19–21], phosphorus materials [22], graphene derivatives [23], and synthetic organic polymers [11,24,25], capable of converting NIR light to generate hyperthermia have been demonstrated to be available for cancer PTT. Among them, the bioinspired polydopamine (PDA) nanoparticles from oxidative self-polymerization of dopamine have been extensively exploited as DDS owing to their simple preparation, good biocompatibility and biodegradation, high photothermal conversion efficiency and excellent combination with functional ligands or therapeutic agents on the surface by multiple interactions [11,25–27]. However, the poor colloidal stability of bare PDA nanoparticles in the physiological environment severely restricted their practical application in cancer nanomedicine.

To improve the colloidal stability of PDA nanoparticles, the frequently employed strategy is to modify the surfaces of PDA nanoparticles with hydrophilic and biocompatible poly(ethylene glycol) (PEG) [11,28]. Also, it has been demonstrated that the surface PEG coating of nanoparticles can significantly reduce their elimination by the reticuloendothelial system (RES), thus prolonging their blood circulation to increase tumor accumulation upon EPR effect [29–32]. Nevertheless, more and more studies revealed that the PEG-rich surfaces of nanovehicles hindered their uptake by cancer cells to some extent, thereby appreciably reducing intracellular drug delivery and antitumor efficacy [33,34]. In order to overcome this PEG dilemma, some strategies of endowing nano-scaled DDS with the capability of detaching PEG shielding in response to tumor extracellular acidity (pH$_e$ 6.3 ~ 7.0) and matrix have emerged recently [34–40]. For instance, acid-labile covalent bonds (e.g. hydrazine, vinyl ether, orthoester, borate-coordination and benzoic-imine) [5,34–37] and matrix metalloproteinase-cleavable peptide [39,40], were incorporated into surface PEG decorations of nanocarriers for tumor site-specific dePEGylation. Liu's group synthesized a pH-sensitive copolymer, PEG-benzoic imine-poly(γ-benzyl-l-aspartate)-b-poly(1-vinylimidazole) block copolymer, to fabricate a pH multistage responsive micelle platform for co-delivery of paclitaxel and curcumin to synergistically kill breast cancer stem cells (bCSCs) and non-bCSCs [34]. After long-term blood circulation and extravasation from leaky blood vessels at tumor regions, the drug-loaded micelles underwent PEG detachment via acidity-triggered hydrolysis of benzoic imine bonds to promote their cellular uptake and deep tumor penetration, thus implementing outstanding tumor inhibition potency and effective bCSCs-killing capacity in vivo. Moreover, as reported by some literatures, the functionalized nano-scaled DDS designed with tumor site-specific dePEGylation and active tumor-targeting ligands could further increase their cellular uptake by tumor cells [11,41–43]. For example, a hyaluronic acid (HA)-based transformable supramolecular nanoassembly with surface modification via host–guest inclusion interaction was developed as vehicle of doxorubicin (DOX), a chemotherapy drug [43]. The in vitro and in vivo data demonstrated that the DOX-carrying supramolecular nanoassemblies exhibited prolonged blood circulation time and effective tumor uptake upon tumor extracellular acidity-elicited detachment of PEG shells and exposure of HA ligands capable of actively targeting CD44 receptor-overexpressed tumor cells, thereby effectively inhibiting tumor growth. Despite of significant development of the polymeric nanoassemblies equipped with tumor site-specific dePEGylation and active tumor-targeting, to the best of our knowledge, very few studies on the PDA-constituted nanoparticles designed with tumor acidity-responsive dePEGylation and active tumor homing were reported [11].

In view of the aforementioned viewpoints, in order to promote tumor-targeted delivery of the photothermal/chemo combined therapy for better antitumor effect, a facile and practical strategy was adopted herein to prepare versatile PDA-containing hybrid nanoparticles capable of selectively delivering DOX to tumor sites and achieving detachment of PEG segments and exposure of folate (FA) ligands, an active tumor targeting moiety, in response to acidic tumor microenvironment (Scheme 1). First, the hydrophilic benzoic imine-containing PEGylated chitosan (BI-PC) as crucial stabilizer was synthesized by the conjugation of chitosan with methoxy PEG benzaldehyde (mPEG-CHO) via Schiff base reaction. Subsequently, the oxidative self-polymerization of dopamine was accompanied with addition of BI-PC adducts to obtain the hybrid BI-PC/PDA nanoparticles. During one-pot co-deposition of BI-PC and DA, through Michael addition between primary amine groups of chitosan segments and 5,6-dihydroxyindole (DHI) units of PDA, the BI-

PC adducts were chemically decorated on the surfaces of a hydrophobic PDA solid core to stabilize hybrid nanoparticles. By the π-π stacking and hydrophobic interactions of DOX with PDA, the DOX-carrying BI-PC/PDA (DOX@BI-PC/PDA) nanoparticles were attained, and exhibited acidity/photothermal-triggered DOX liberation and outstanding photothermal conversion efficiency (ca. 43.1 %). Next, FA molecules were covalently conjugated on the surfaces of DOX@BI-PC/PDA nanoparticles upon Michael addition. The resulting FA-DOX@BI-PC/PDA nanoparticles were appreciably internalized by FA receptor-overexpressed CT-26 colon cancer cells under mimic tumor acidic condition via acidity-elicited PEG detachment and FA exposure, thus augmenting anticancer potency of the photothermal/chemo therapy. More importantly, the pH_e-responsive FA-DOX@BI-PC/PDA nanoparticles markedly accumulated in tumor sites upon the enhanced internalization by CT-26 cancer cells and executed superior NIR-activated hyperthermia, thus prominently inhibiting tumor growth by combining with DOX chemotherapy.

2. Materials and methods

2.1. Materials

Dopamine·hydrochloride (DA) was acquired from Alfa Aesar (USA). Tris(hydroxymethyl) aminomethane (99% for biochemistry) were supplied by Acros Organics (USA). DOX·HCl was purchased from Carbosynth Ltd. (UK). Chitosan oligosaccharide (MW 5.0 kDa, 81 % degree of deacetylation) was obtained from Glentham Life Science Ltd. (UK). Methoxy PEG (mPEG) (MW 5.0 kDa), folic acid (FA), 3-(4,5-Dimethylthiazol-2-yl)-2,5-diphenyltetrazolium bromide (MTT), dulbecco's modified Eagle medium (DMEM), RPMI-1640 medium, and D_2O (99.9 atom % D) were purchased from Sigma-Aldrich (USA). Fetal bovine serum (FBS) was obtained from Hyclone (USA). Hoechst 33,342 was purchased from Invitrogen. Deionized water was produced from Milli-Q Synthesis (18 MΩ, Millipore). All other chemicals were reagent grade and used as received. TRAMP-C1 cells (murine prostate cancer cell line), CT-26 cells (murine colon adenocarcinoma cell line) were acquired from Food Industry Research and Development Institute (Hsinchu City, Taiwan).

2.2. Synthesis and characterization of BI-PC adducts

The mPEG-CHO utilized in this work was attained by our previous method [36]. mPEG-CHO (40, 80 or 120 mg) dissolved anhydrous DMSO (2.0 mL) was added into DMSO (3.0 mL) containing chitosan (200 mg). The reaction was performed under stirring at 25 °C for 24 h, followed by dialysis (Cellu Sep MWCO 6000 ~ 8000) against pH 8.0 phosphate buffer to remove residual mPEG-CHO, chitosan and DMSO. The final product was collected by lyophilization. The degree of substitution (DS) of chitosan with mPEG-CHO defined here as the number of mPEG segments per 100 glucosamine units was determined by ^{1}H NMR in D_2O at 25 °C. The chemical structure of BI-PC adducts was also characterized by Fourier transform infrared (FT-IR) spectroscopy (FT-720, HORIBA, Japan) using KBr pellet for the sample preparation. Furthermore, the BI-PC adducts were dissolved in pH 6.5 aqueous solution and then stirred for 24 h at 37 °C. Next the acidity-treated BI-PC adducts were freeze dried and characterized by ^{1}H NMR to observe the hydrolysis of benzoic imine bonds in BI-PC adducts.

2.3. Preparation of hybrid BI-PC/PDA nanoparticles

BI-PC (0.7, 1.4 or 2.8 folds with respect to weight of DA residues in feed) dissolved in 0.2 M tris buffer was added into DA-containing co-solvent (3.5 mg/mL) comprising ethanol and deionized water of 4:3 (v/v). The solution was stirred in dark at room temperature for 24 h to obtain hybrid BI-PC/PDA nanoparticles, followed by dialysis (Cellu Sep MWCO 12000 ~ 14000) against pH 8.0 phosphate buffer at 4 °C to remove unreacted DA, BI-PC and ethanol. For comparisons, the chitosan/PDA nanoparticles and PDA nanoparticles were prepared, respectively, in a similar manner.

2.4. DOX loading and FA conjugation

Due to the weak base property of DOX molecules (pka 8.6), in order to promote drug loading content of BI-PC/PDA nanoparticles, the DOX loading was performed in phosphate buffer of pH 8.0 where the water solubility of DOX was reduced, thus enhancing the hydrophobic and π-π stacking interactions between DOX and PDA. For DOX loading and FA decoration, DOX hydrochloride dissolved DMSO (3.2 mg/mL, 0.25 mL) was added dropwise into pH 8.0 phosphate buffer containing BI-PC/PDA nanoparticles (2.3 mg/mL, 1.75 mL) under stirring. The solution was then stirred in dark at room temperature for 24 h and dialyzed against pH 8.0 phosphate buffer at 4 °C to remove unloaded DOX molecules and DMSO. Furthermore, to decorate the surfaces of DOX@BI-PC/PDA nanoparticles with FA molecules, FA (0.24 mg) was dissolved in 0.22 mL DMSO and added dropwise into the DOX@BI-PC/PDA nanoparticle solution (2.3 mg/mL, 1.78 mL) under stirring. The mixture was stirred in dark at room temperature for 6 h, followed by dialysis (Cellu Sep MWCO 12000 ~ 14000) against pH 8.0 phosphate buffer at 4 °C to remove unreacted FA and DMSO.

2.5. ICG encapsulation

For ICG encapsulation, ICG dissolved in DMSO (0.8 mg/mL, 0.25 mL) was added dropwise into pH 8.0 phosphate buffer containing FA-BI-PC/PDA nanoparticles (2.3 mg/mL, 1.75 mL) under stirring. The obtained solution was then stirred in dark at room temperature for 24 h and dialyzed (Cellu Sep MWCO 12000 ~ 14000) against pH 8.0 phosphate buffer at 4 °C to remove unloaded ICG molecules and DMSO. To quantify ICG encapsulated within hybrid nanoparticles, a prescribed volume of ICG-encapsulated nanoparticle solution was lyophilized and then dissolved in DMSO to extract the drug. The absorbance of ICG at 794 nm was determined by a UV/Vis spectrophotometer (U-2900, Hitachi).

2.6. Nanoparticle characterization

The absorption spectra of DA molecules, PDA and DOX@BI-PC/PDA nanoparticles in pH 8.0 phosphate buffer were attained using a UV/Vis spectrophotometer (U2900, Hitachi, Japan). X-ray photoelectron spectroscopy (XPS) analysis was achieved by a PHI 5000 VersaProbe III X-ray photoelectron spectrometer (ULVAC-PHI, Japan) with AlKα radiation ($h\gamma$ = 1486.6 eV) at 15 kV and 150 W. Thermogravimetric analysis (TGA) was conducted with Thermo Scientific Cahn TGA Versa Therm-HS in an N_2 atmosphere by heating the sample to 900 °C at the rate of 10 °C/min. The particle size and size distribution of various PDA-based nanoparticles in aqueous solutions of different pH values were determined by dynamic light scattering (DLS) using a Brookhaven BI-200SM goniometer equipped with a BI-9000 AT digital correlator using a solid-state laser (35 mW, λ = 637 nm) detected at a scattering angle of 90°. The data presented herein represent an average of at least triplicate measurements. To get insight into the morphology of BI-PC/PDA and DOX@BI-PC/PDA nanoparticles in aqueous solutions at pH 7.4 and 5.0, respectively, in addition to the angular dependence of the autocorrelation functions, the ratio of the root-mean-square radius of gyration (R_g) to the mean hydrodynamic radius (R_h) of these nanoparticles was obtained by angular dependent dynamic and static light scattering (DLS/SLS) measurements using the aforementioned instrument. The R_g of PDA-based nanoparticles was quantitatively determined using Berry plot of the scattering intensity ($I_{ex}^{-1/2}$) versus the square of the scattering vector (q^2) from the angle-dependent measurements of the light scattering intensity. The zeta potential of the nanoparticles in aqueous solutions of various pH was measured with a Litesizer 500 (Anton Paar, USA). Fourier-transform infrared spectroscopy (FT-IR) spectra of PDA

and BI-PC/PDA nanoparticles were acquired using a FT-IR spectrometer (HORIBA FT-720). The dried sample pressed with KBr was scanned from 4000 to 400 cm^{-1}. The morphology of various PDA-based nanoparticles was attained by transmission electron microscope (TEM) (HT7700, Hitachi, Japan) and scanning electron microscope (SEM) (JEOL JSM-7800F Prime Schottky Field Emission SEM, Japan). Various PDA-based nanoparticles in PBS (1.0 mL) were irradiated by a NIR laser of 808 nm (1.0 W/cm^2) for 5 min. The infrared thermographic maps and solution temperatures were recorded with an infrared thermal imaging camera (Thermo Shot F20, NEC Avio Infrared Technologies, Germany). To explore the photostability, the PDA and DOX@BI-PC/PDA nanoparticle solution (PDA concentration: 200 μg/mL) were irradiated by 808 nm NIR laser (1.0 W/cm^2) for 5 min and then cooled down to room temperature (in 5 min) by turning off the light source. The heating/cooling procedure was repeated three times. Based on the data from the cooling status, the photothermal conversion efficiency was also obtained.

To quantify DOX encapsulated within nanoparticles, a preset volume of DOX@BI-PC/PDA solution was lyophilized and then dispersed in DMSO for effective drug isolation from nanoparticles. Next, the solution was centrifuged to withdraw the supernatant for analysis. The DOX fluorescence in the range 500–700 nm was measured by a fluorescence spectrometer (F-2700, Hitachi, Japan). The drug loading efficiency (DLE) and loading content (DLC) were calculated by the following formulas:

$$\text{DLE (\%)} = (\text{weight of DOX loaded/weight of DOX in feed}) \times 100\%$$

$$\text{DLC (\%)} = (\text{weight of DOX loaded/total weight of DOX-carrying nanoparticles}) \times 100\%$$

For in vitro DOX release test, the DOX@BI-PC/PDA nanoparticle dispersion (1.0 mL) was dialyzed (Cellu Sep MWCO 12000–14000) against PBS (pH 7.4) and acetate buffer (pH 5.0) (25 mL) at 37 °C, respectively. At prescribed time intervals, 1.0 mL of dialysate (pH 5.0 or 7.4) was withdrawn for analysis and replaced with an equal volume of fresh buffer. Moreover, to evaluate the effect of NIR-triggered hyperthermia of DOX@BI-PC/PDA nanoparticles on their drug release, at 1, 3, and 6 h post incubation, the internal sample in each pH group was withdrawn and irradiated by 808 nm NIR laser for 5 min. All samples were continuously incubated up to 24 h. The amount of DOX released was determined by fluorescence measurements as described above.

2.7. In vitro cellular uptake

CT-26 cells (1.5×10^5 cells/well) seeded onto 22 mm round glass coverslips in 6-well plates were incubated with free DOX, DOX@BI-PC/PDA and FA-DOX@BI-PC/PDA nanoparticles (DOX concentration = 10 μM) at pH 7.4 and 6.5, respectively, for 4 h. After being washed three times with HBSS and immobilized with 4 % formaldehyde, the cell nuclei were stained with Hoechst 33342. The cellular images were gained by confocal laser scanning microscope (CLSM) (LSM-800, Zeiss, Germany) equipped with a Hoechst set (Ex. 360 nm and Em. 461 nm) and a DOX set (Ex. 488 nm and Em. 555 nm). Furthermore, the FACSCalibur flow cytometer (BD Bioscience) was employed to evaluate cellular uptake of DOX@BI-PC/PDA and FA-DOX@BI-PC/PDA nanoparticles (DOX concentration = 10 μM) by CT-26 cells at 37 °C and at pH 7.4 and 6.5. After 4 h incubation and detachment with trypsin-EDTA solution, the treated CT-26 cells (2×10^5 cells/well) were suspended in PBS (1.0 mL) to obtain a cell suspension containing a minimum of 1×10^4 cells.

2.8. In vitro photothermal/chemo anticancer efficacy

CT-26 cells (1×10^5 cells/well) were seeded in a 6-well plate and incubated at 37 °C for 24 h in RPMI containing 10% FBS and 1% penicillin. The medium was then replaced with 1.0 mL of fresh medium containing free DOX or various nanoformulations and was incubated at pH 7.4 and 6.5 for additional 24 h. After being washed twice with PBS, cells were detached with trypsin-EDTA and centrifuged (1500 rpm). The obtained cell pellets were dispersed in RPMI (150 μL) and then irradiated with NIR 808 nm laser (1.25 W/cm^2) for 5 min. The laser-treated cells were reseeded in a 12-well plate and re-incubated for 12 h. MTT (0.25 mg/mL, 1.0 mL) was then added into each well, followed by incubation at 37 °C for 3 h. After discarding the culture medium, DMSO (1.0 mL) was added to dissolve the precipitate and the absorbance of the resulting solution at 570 nm was measured using a BioTek 800TS microplate reader. The viability of CT-26 cells treated with free DOX and different nanoformulations in the absence of NIR laser irradiation was also assessed in a similar manner.

2.9. Live and dead cell assay

CT-26 cells (1.5×10^5 cells/well) were seeded in a 12-well plate and incubated at 37 °C for 24 h in RPMI containing 10% FBS and 1% penicillin. The medium was then replaced with 1.0 mL of fresh medium containing BI-PC/PDA nanoparticles (200 μg/mL) was incubated at pH 7.4 and 6.5 for additional 24 h. After that, cells were exposed to the 808 nm NIR laser (1.25 W/cm^2) for 5 min and gently washed with PBS twice to avoid washing off dead cells. Calcein AM (0.2 μM) and propidium iodide (PI, 25 μg/mL) mixture solution (500 μL) was added and kept at room temperature for 30 min. The cellular images were attained using a NIB-100F inverted fluorescent biological microscope (Nanjing Jiangnan Novel Optics Co., Ltd., China).

2.10. Animals and tumor model

Female BALB/c mice (6 ~ 8 weeks old) were purchased from National Laboratory Animal Center (Taiwan). Animals received care in accordance with the Guidance Suggestions for the Care and Use of Laboratory Animals, approved by the Administrative Committee on Animal Research in the Chung Shan Medical University (Taiwan) (IACUC Approval No: 2528). For establishing tumor model, 5×10^6 CT-26 cells were subcutaneously injected into the right thigh of mice. After one week post-inoculation, the tumor model was established. Tumor volume (V) was calculated as follows: $V = L \times W^2/2$, where W is the tumor measurement at the widest point and L the tumor dimension at the longest point.

2.11. In vivo imaging and biodistribution

When the tumor volume reached 80 ~ 110 mm^3, PBS, free ICG and various ICG-labeled hybrid nanoparticles were injected, respectively, into the mice via tail vein at a dosage of 0.3 mg/kg ICG. The fluorescence signals of ICG (Ex. 710 nm and Em. 760 nm) at 2, 4, 6 and 24 h post-injection were collected with an IVIS imaging system (IVIS Lumina II, Caliper, LifeSciences, MA, USA). The treated mice were sacrificed at 48 h post-injection and the major organs and tumor were harvested for individual organ imaging by IVIS.

2.12. In vivo temperature measurements upon NIR irradiation

The procedure for the in vivo distribution evaluation was followed. At 6 h post-injection, the tumor region of mice was irradiated by the 808 nm laser with a power density of 1.25 W/cm^2 for 5 min. The infrared thermographic maps of mice and the tumor local temperature during NIR laser irradiation were attained with infrared thermal imaging camera (Thermo Shot F20, NEC Avio Infrared Technologies, Germany).

2.13. In vivo tumor growth inhibition

When tumor volume of mice reached 80 ~ 110 mm^3, mice were randomly divided into 7 groups and injected intravenously with PBS,

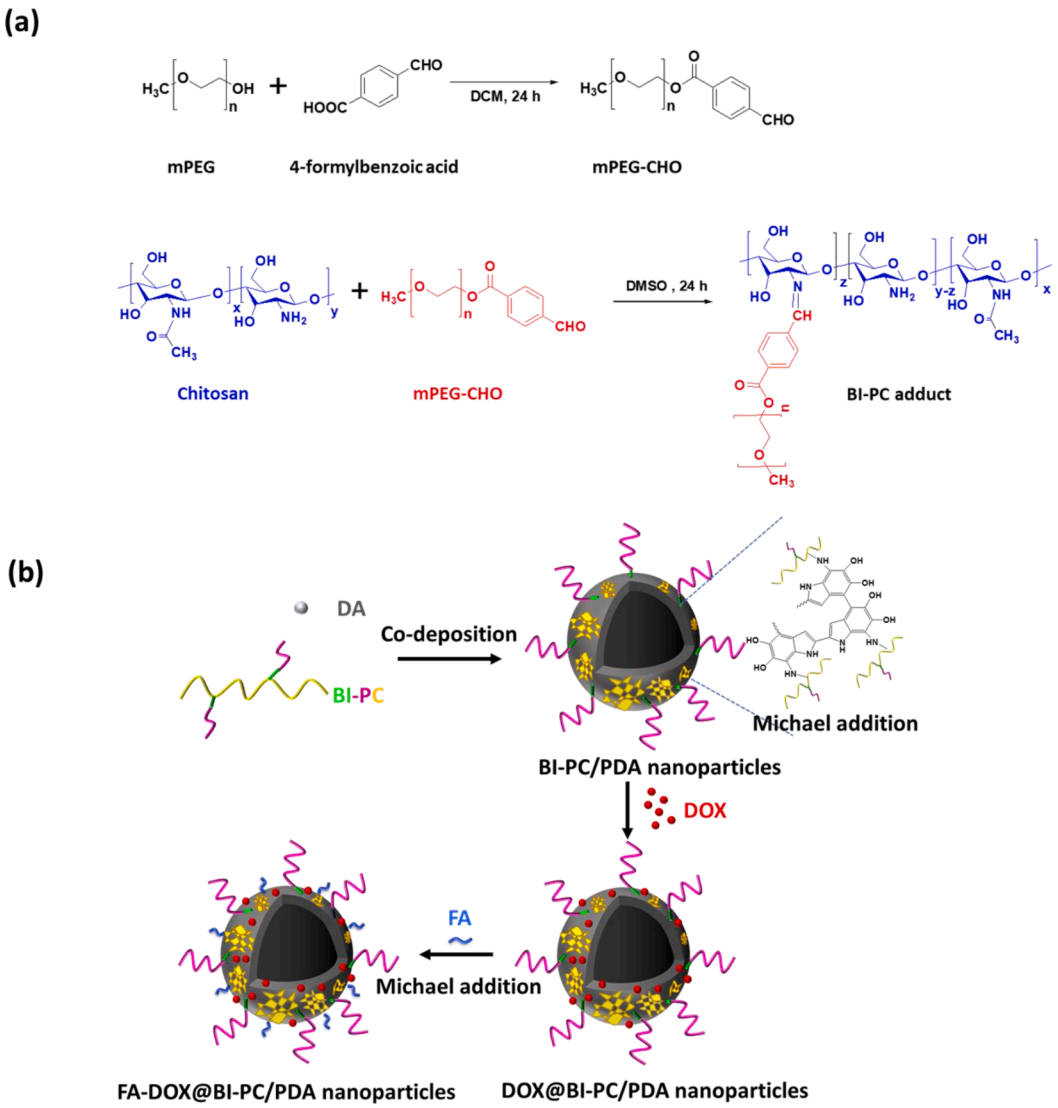

Scheme 2. (a) Synthetic route and chemical structure of BI-PC adducts. (b) Illustration of strategy to fabricate FA-DOX@BI-PC/PDA nanoparticles.

free DOX, FA-BI-PC/PDA, DOX@BI-PC/PDA and FA-DOX@BI-PC/PDA nanoparticles at a dosage of 1.4 mg/kg DOX. Each group was treated with a total of two doses at days 0 and 2. Six h post-injection, the mice receiving FA-BI-PC/PDA, DOX@BI-PC/PDA and FA-DOX@BI-PC/PDA nanoparticles (5 in each group) were irradiated at the tumor sites with 808 nm laser (1.25 W/cm^2) for 5 min. The tumor volumes and body weight of various groups were measured every two days until 14 days post-injection. The tumors were then isolated from the euthanized mice and weighted for therapeutic index (TI) measurements. Sections of tumors and major organs of pertinent sizes were stained with H&E and Ki67, and examined by an Olympus IX70 inverted microscope (Japan).

2.14. Statistical analysis

Data are reported as mean ± SD. The differences among groups were determined using one-way or two-way ANOVA analysis; ns > 0.05, *$p < 0.05$, **$p < 0.01$, ***$p < 0.001$.

3. Results and discussion

3.1. Synthesis and characterization of BI-PC adducts

The BI-PC adducts utilized in this study were synthesized by Schiff base reaction of chitosan with mPEG-CHO as illustrated in Scheme 2a. Compared with the ^{1}H NMR spectra of chitosan and mPEG-CHO (Fig. 1a and b), the presence of proton signals of ethylene groups of mPEG at δ 3.7 ppm, and of imine groups at δ 8.5 ppm, and the complete disappearance of the proton signals of aldehyde groups at δ 10.1 ppm were observed in the ^{1}H NMR spectrum of BI-PC adducts (Fig. 1c), confirming the successful conjugation of chitosan with mPEG-CHO. Based on the signal integral ratio of the methoxy protons (δ 3.4 ppm) of mPEG-CHO and the H2 protons (δ 2.7 ppm) from glucosamine residues of chitosan, the DS of chitosan with mPEG-CHO was calculated to be ca 11.7. For comparison, the BI-PC adducts with different DS values were also prepared in a similar way and characterized by ^{1}H NMR measurement (Fig. S1). In agreement with the ^{1}H NMR data, the FT-IR spectrum of BI-PC adducts also showed the feature bands at 1115 and 1649 cm^{-1} ascribed to the C-O and C = N stretching vibration of ethylene glycol residues and imine linkages, respectively (Fig. S2). Importantly, as presented in the ^{1}H NMR spectrum of BI-PC adducts (DS: 11.7) after acid treatment (Fig. 1d), the complete disappearance of proton signals of imine group at δ 8.5 ppm and the appearance of proton signals of aldehyde group at δ 10.1 ppm convincingly demonstrate the acidity-elicited hydrolysis of benzoic imine bonds within BI-PC adducts.

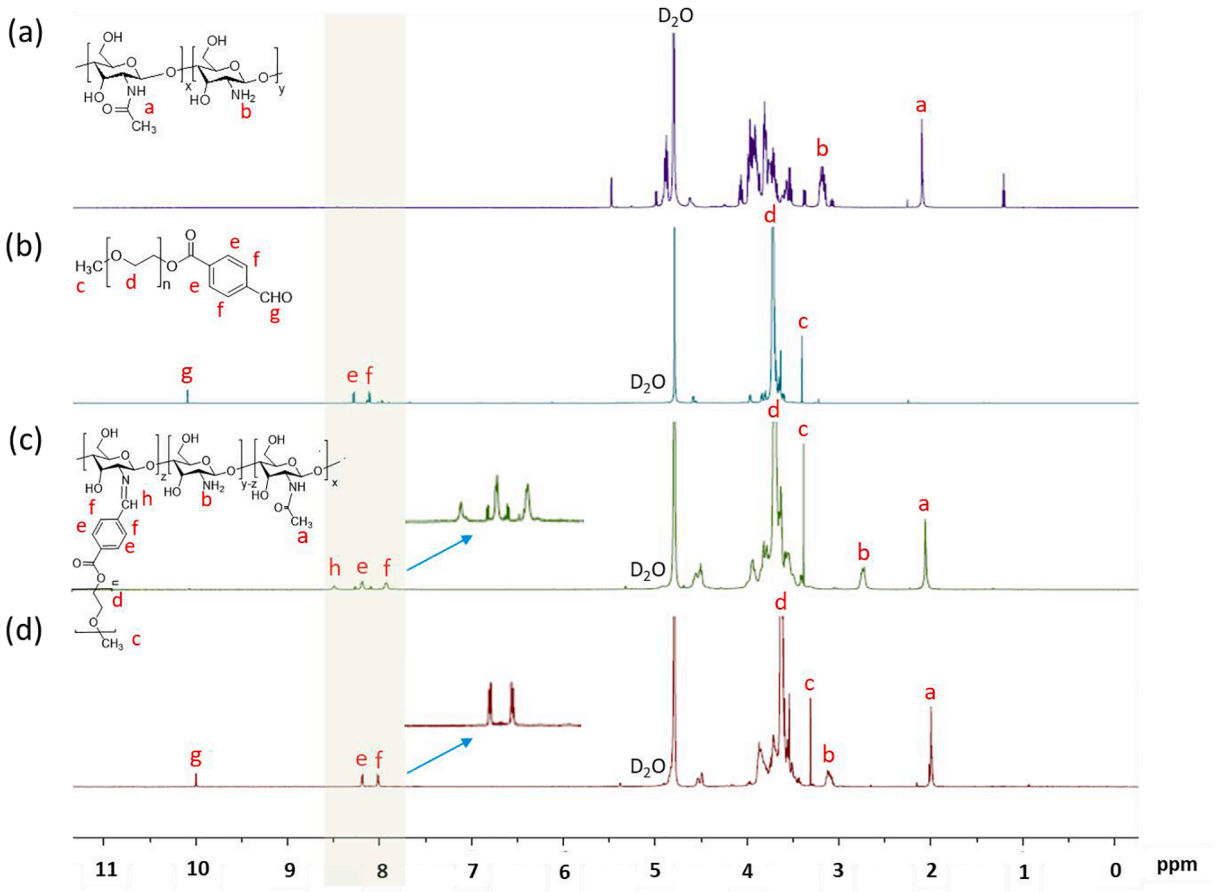

Fig. 1. ^{1}H NMR spectra of (a) chitosan, (b) mPEG-CHO, (c) BI-PC (DS: 11.7) and (d) acidity-treated BI-PC (DS: 11.7) in D_2O.

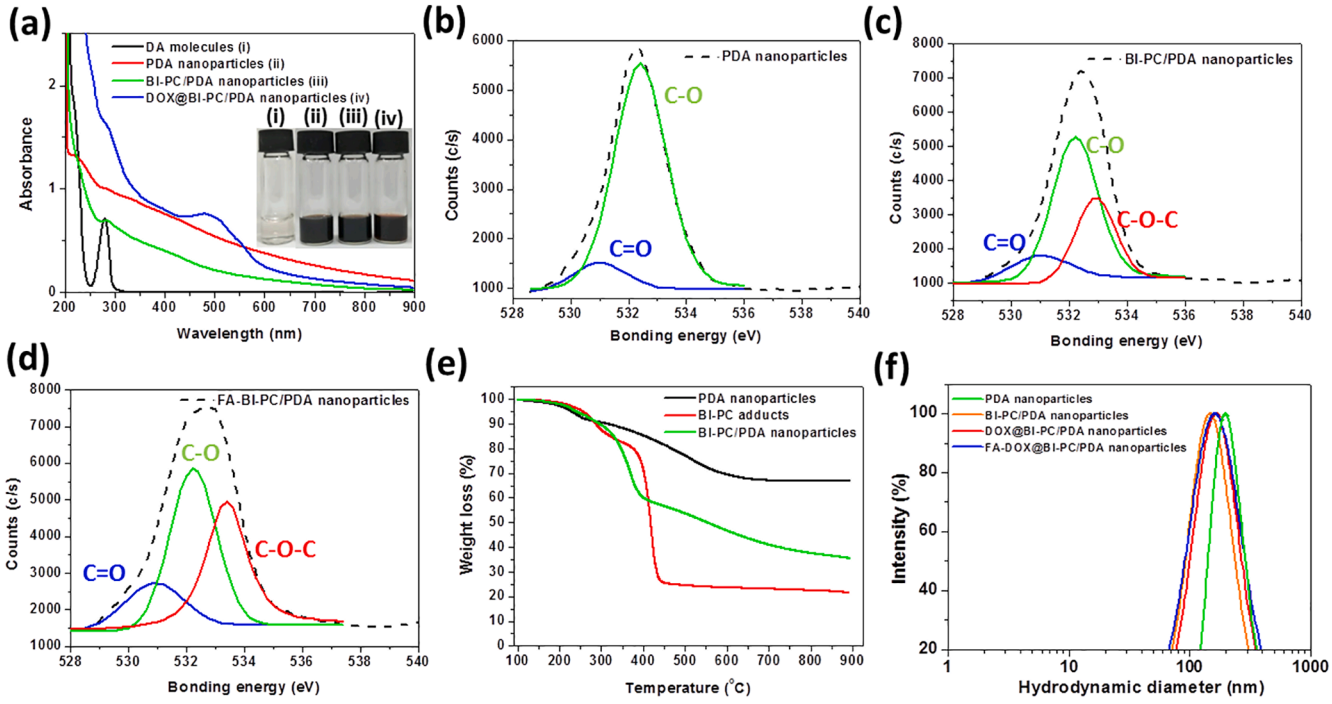

Fig. 2. (a) UV/Vis spectra of DA molecules, PDA, BI-PC/PDA and DOX@BI-PC/PDA nanoparticles in aqueous solution. XPS spectra of (b) PDA nanoparticles, (c) BI-PC/PDA nanoparticles and (d) FA-BI-PC/PDA nanoparticles. (e) TGA profiles of BI-PC adducts, PDA and BI-PC/PDA nanoparticles. (f) DLS particle size distribution profiles of PDA, BI-PC/PDA, DOX@BI-PC/PDA and FA-DOX@BI-PC/PDA nanoparticles in pH 7.4 PBS.

Table 1
DLS data and drug loading characterics of PDA-based nanoparticles.

Sample	D_h (nm)	PDI	DLE (%)	DLC (wt %)
PDA nanoparticles	272.1 ± 10.2	0.135	–	–
BI-PC/PDA nanoparticles	146.6 ± 3.7	0.169	–	–
DOX@BI-PC/PDA nanoparticles	158.8 ± 8.0	0.219	88.1 ± 2.7	15.0 ± 0.1
FA-DOX@BI-PC/PDA nanoparticles	161.1 ± 3.6	0.266	82.1 ± 3.7	14.8 ± 0.3

3.2. Preparation and characterization of pH_e-sensitive PDA-containing nanoparticles

In order to develop the tumor acidity-triggered PEG detachable PDA nanoparticles as DOX vehicles, the hybrid BI-PC/PDA nanoparticles were fabricated by one-pot co-deposition of acidity-responsive BI-PC adducts (DS: 11.7) and DA molecules at a weight ratio of 1.4:1 in Tris-containing aqueous solution. Based on Michael addition between primary amine groups of chitosan segments with DHI units of PDA, it was presumed that the hydrophilic BI-PC adducts employed as stabilizing agent could be covalently coupled with PDA during co-deposition of BI-PC and DA (Scheme 2b). For comparison, the unmodified PDA nanoparticles and hybrid chitosan/PDA nanoparticles without PEGylation were also prepared. As shown in the UV/Vis spectra (Fig. 2a), distinct from the appearance of feature absorption peak (281 nm) of DA molecules in aqueous solution, in addition to the enhanced absorption from 300 to 800 nm, no significant feature absorption peak was observed for PDA nanoparticles and BI-PC/PDA nanoparticles. Moreover, the aqueous solutions containing DA or BI-PC/DA mixture gradually turned from the transparent to black state under basic reaction condition. These results clearly illustrate that the DA monomers in Tris-containing aqueous solution can sufficiently self-polymerize into PDA, even in the presence of BI-PC adducts. Also, as presented in the XPS spectra (Fig. 2b and c), in addition to the feature peaks of C = O (531.0 eV) and C-O (532.5 eV) from PDA nanoparticles, the new peak of C-O-C (533.0 eV) from BI-PC adducts was observed for hybrid BI-PC/PDA nanoparticles, demonstrating the successful combination of BI-PC adducts with PDA nanoparticles. The TGA profiles further showed that the hybrid BI-PC/PDA nanoparticles were composed of ca. 70.2 wt% BI-PC and 29.8 wt % PDA (Fig. 2e). Based on the characterization of hybrid nanoparticles by DLS, the BI-PC/PDA nanoparticles exhibited mean hydrodynamic diameters (D_h) of ca 146.6 nm and narrow size distributions (PDI ca 0.169) in phosphate buffer saline (PBS, pH 7.4, I = 0.15 M) (Fig. 2f and Table 1).

For the BI-PC/PDA nanoparticles, the angle-dependent DLS data revealed a high linear relationship between the relaxation frequency (Γ) and the square of the scattering vector (q^2) (Fig. 3a), being indicative of their spherical particle shape [44]. This is consistent with the well-dispersed and spherical form of BI-PC/PDA nanoparticles observed by TEM and SEM (Fig. 3c and e). It should be noted that the particle size (ca 146.6 nm) of BI-PC/PDA nanoparticles determined by DLS is somewhat larger compared to that (ca 96.5 nm) of those observed by TEM due to their structural transition from hydrated (DLS) to dry (TEM) state. To get insight into the molecular packing architecture of BI-PC/PDA

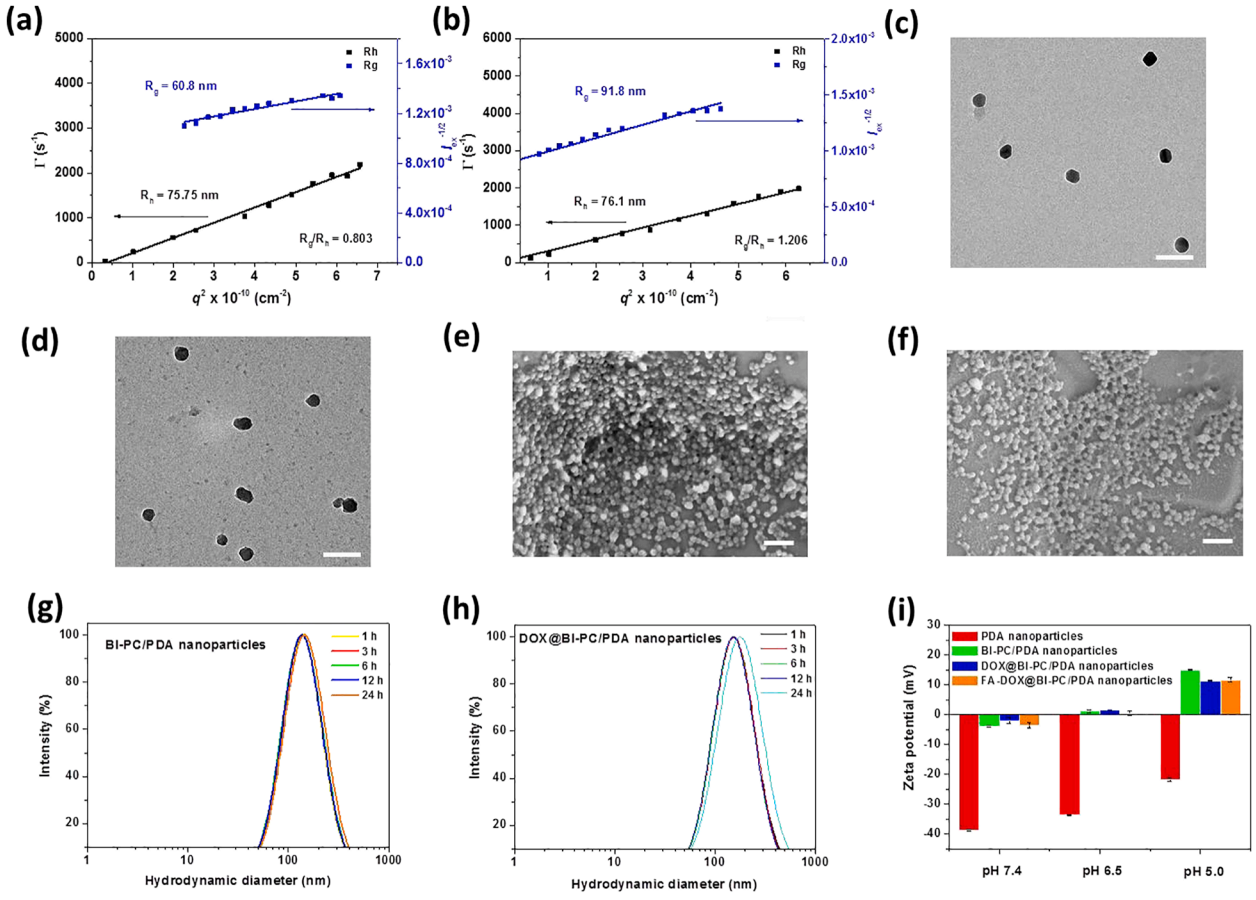

Fig. 3. Berry plot for R_g and angle dependent correlation function of R_h of BI-PC/PDA nanoparticles in (a) pH 7.4 PBS and (b) pH 5.0 acetate buffer. TEM images of (c) BI-PC/PDA nanoparticles and (d) DOX@BI-PC/PDA nanoparticles. Scale bars are 200 nm. SEM images of (e) BI-PC/PDA nanoparticles and (f) DOX@BI-PC/PDA nanoparticles. Scale bars are 1 μm. DLS particle size distribution profiles of (g) BI-PC/PDA nanoparticles and (h) DOX@BI-PC/PDA nanoparticles in PBS containing 10 % FBS at different time intervals. (i) Zeta potential of various PDA-based nanoparticles in aqueous solutions at different pH.

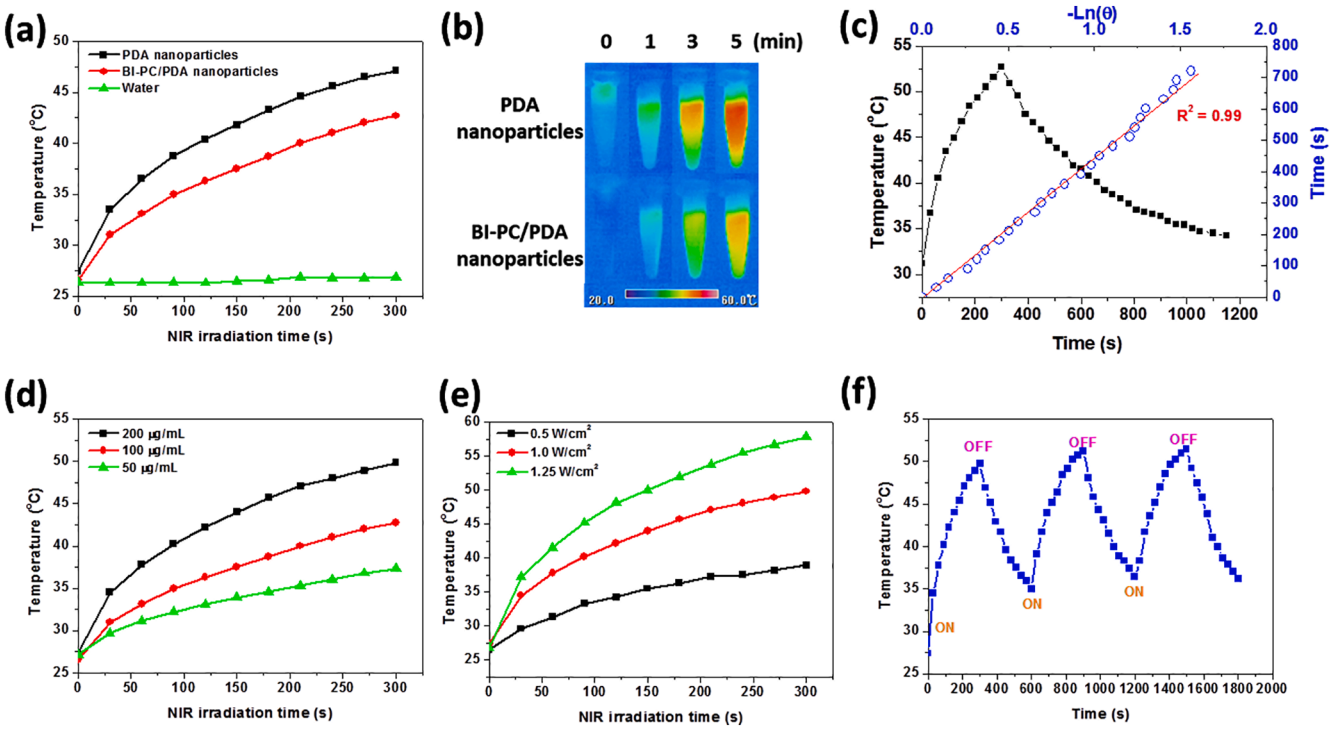

Fig. 4. (a) Temperature profiles and (b) thermal images of PDA and BI-PC/PDA nanoparticles (PDA concentration: 100 μg/mL) in aqueous solution with 808 nm NIR laser irradiation (1.0 W/cm^2). (c) Temperature profile of BI-PC/PDA nanoparticle solution (PDA concentration: 200 μg/mL) after exposure to 808 nm laser irradiation (1.0 W/cm^2) for single on/off cycle, and plot of cooling time versus negative logarithm of the temperature driving force. (d) Temperature profiles of BI-PC/PDA nanoparticles of different PDA concentrations in PBS under 808 nm NIR laser irradiation (1.0 W/cm^2). (e) Temperature profiles of BI-PC/PDA nanoparticles (PDA concentration: 200 μg/mL) in PBS under 808 nm NIR laser irradiation of different power densities. (f) Temperature change of each heating cycle of BI-PC/PDA nanoparticle solution (PDA concentration: 200 μg/mL) exposed to irradiation of 808 nm NIR laser (1.0 W/cm^2).

nanoparticles in pH 7.4 PBS, their R_g was determined by angle-dependent SLS as presented in Fig. 3a. The R_g/R_h ratio that is sensitive to assembly morphology was thus acquired to be 0.803, being close to that (0.775) of uniform rigid spheres [44–46]. Considering the inherent hydrophilic property of BI-PC and water-insoluble nature of PDA, the hybrid BI-PC/PDA nanoparticles were characterized to have a spherical core–shell structure composed of a hydrophobic PDA core surrounded by hydrated BI-PC shell (Scheme 2b). Furthermore, compared to the BI-PC/PDA nanoparticles, the pristine PDA nanoparticles in PBS displayed significantly larger particle size (ca 272.1 nm) (Fig. 2f and Table 1). Note that, distinct from the considerably enlarged particle size of PDA nanoparticles suspended in pH 7.4 PBS at 37 °C over 24 h, the BI-PC/PDA nanoparticles maintained virtually unchanged particle size under the same condition (Fig. S3). Apparently, due to the lack of hydrophilic BI-PC surface decoration, the PDA nanoparticles inclined to aggregate into huge particles in 0.15 M PBS. Such a remarkable aggregation of PDA nanoparticles in aqueous solutions with salt concentration beyond 10 mM was also observed elsewhere [28,47–49]. For this reason, bare PDA is not suitable for in vivo anti-tumor studies. Importantly, the BI-PC/PDA nanoparticles dispersed in 10 % FBS-containing PBS mimicking physiological condition at 37 °C retained nearly unvaried particle size for 24 h (Fig. 3g). The above results suggest that the hydrophilic BI-PC surface decoration could endow hybrid BI-PC/PDA nanoparticles with outstanding colloidal stability, a critical perquisite for reduced RES-mediated clearance and prolonged blood circulation of nanoparticles.

On the other hand, the zeta potential value of BI-PC/PDA nanoparticles in aqueous solution of pH 7.4 determined to be ca −3.9 mV was significantly lower than that (ca −38.7 mV) of PDA nanoparticles (Fig. 3i). This illustrates that the outer PEG segments of BI-PC/PDA nanoparticles could efficiently screen the negative charges from phenol groups of PDA cores. Notably, with the medium pH being adjusted from 7.4 to 5.0, in addition to appreciable increase in R_g/R_h value from 0.803 to 1.206 (Fig. 3a and b), conversions in zeta potentials of BI-PC/PDA nanoparticles from slightly negative (-3.9 mV) to positive values (+15.0 mV) were attained (Fig. 3i). These data signify that the acidity-triggered protonation of chitosan segments and PEG detachment via hydrolysis of benzoic imine linkers lead to the exposure of more positive charges on the surfaces of hybrid nanoparticles. Also, the development of ionic osmotic pressure gradient elicited by immobilized positively-charged chitosan segments of hybrid nanoparticle surfaces facilitates water influx, thereby giving rise to nanoparticles somewhat swollen and loose.

When the weight ratio of BI-PC adducts (DS: 11.7) and DA molecules in feed was adjusted from 2.8:1 to 0.7:1, in addition to the appreciably enlarged particle size and size distribution from DLS characterization (Fig. S4a), a severe aggregation of the resulting BI-PC/PDA nanoparticles was observed in their SEM images (Fig. S4b). This indicates that the BI-PC/PDA nanoparticles from co-deposition of DA molecules with little BI-PC adducts are apt to aggregate in aqueous phase due to their poor colloidal stability in the absence of sufficient hydrophilic BI-PC coatings. Also, at the same BI-PC/DA weight ratio (1.4:1), with the DS value of BI-PC adducts being decreased from 11.7 to 4.7, the particle size of the obtained BI-PC/PDA nanoparticles in PBS was remarkably increased from 146.6 nm to over 1 μm (Table S1 and Fig. S5a), corresponding to a substantial aggregation of BI-PC (DS: 4.7)/PDA nanoparticles observed in their SEM images (Fig. S5b). Furthermore, regardless of the weight ratio of chitosan and DA used in this work, the chitosan/PDA assemblies from co-deposition of chitosan and DA tended to form considerably visible sediment in aqueous solution (Fig. S6). In view of the above findings, it can be concluded that the adequate amount of PEG segments on the surface of hybrid BI-PC/PDA nanoparticles plays an important role in effectively preventing interparticle aggregation to promote colloidal stability. Therefore, the acidity-

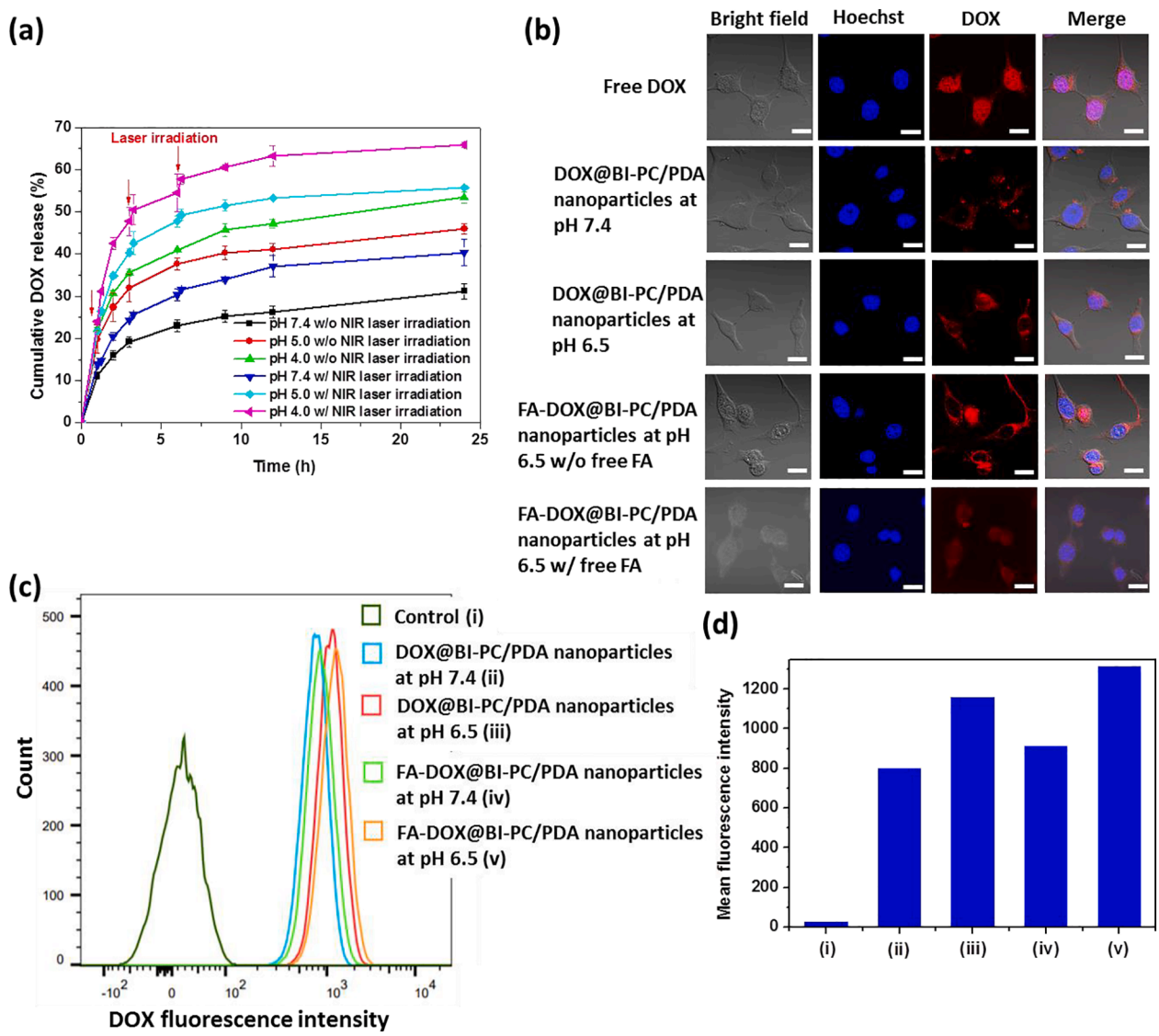

Fig. 5. (a) Cumulative DOX release profiles of DOX@BI-PC/PDA nanoparticles in aqueous solutions of pH 7.4, 5.0 and 4.0 in the presence or absence of NIR laser irradiation of 1.0 W/cm^2. (b) CLSM images of CT-26 cells incubated with either DOX@BI-PC/PDA nanoparticles at pH 7.4 and 6.5 or FA-DOX@BI-PC/PDA nanoparticles at pH 6.5 with and without free FA addition for 4 h (DOX concentration = 10 μM). Scale bars are 20 μm. (c) Flow cytometric histograms and (d) mean DOX fluorescence intensity of CT-26 cells incubated with FA-DOX@BI-PC/PDA and DOX@BI-PC/PDA nanoparticles at pH 7.4 and 6.5 for 4 h (DOX concentration = 10 μM).

responsive BI-PC/PDA nanoparticles fabricated by one-step co-deposition of BI-PC (DS: 11.7) and DA at a BI-PC/DA weight ratio of 1.4:1 were selected as DOX vehicles due to their small particle size and superior colloidal stability suitable for EPR-based tumor-targeted drug delivery.

3.3. NIR-activated photothermal effect

As presented in the UV/Vis spectra (Fig. 2a), the BI-PC/PDA nanoparticles exhibited broad-band monotonic UV/Vis absorption spectrum, thus appearing more like inorganic materials rather than organic. Similar UV/Vis spectra were also observed in other PDA-containing nanomaterials [27,28]. Due to the inherent photothermal effect of PDA nanoparticles, the BI-PC/PDA nanoparticles were expected to effectively absorb light from the UV to NIR ends of the spectrum and convert it into heat through non-radiative decay. To evaluate the feasibility of BI-PC/PDA nanoparticles in application of cancer PTT, their NIR-triggered photothermal effect was explored by monitoring the temperature changes of hybrid nanoparticle solutions under NIR laser irradiation of 808 nm. As presented in Fig. 4a and b, upon NIR laser irradiation (power density of 1.0 W/cm^2) for 300 s, compared to nearly unvaried temperature (ca 27 °C) of PBS, the temperatures of aqueous solutions containing either PDA nanoparticles or BI-PC/PDA nanoparticles at the same PDA concentration (100 μg/mL) were remarkably raised from 27 °C to 47 and 43 °C, respectively. According to the photothermal heating–cooling curve (Fig. 4c) and a reported method [50,51], the photothermal conversion efficiencies (η) of BI-PC/PDA nanoparticles were attained to be ca. 43.1 % comparable to that (ca. 39.5 %) of PDA nanoparticles (Fig. S7). This indicates that the BI-PC surface decoration could not affect the photothermal conversion capability of PDA nanoparticles. Also, the BI-PC/PDA nanoparticles displayed NIR-triggered hyperthermia ability in the concentration-dependent and a laser power density-dependent manner (Fig. 4d and e). It is worth mentioning that, after three cycles of continuous NIR laser irradiation, the BI-PC/PDA nanoparticles still maintain not only sound NIR-triggered hyperthermia ability (Fig. 4f) but also nearly unchanged particle size, zeta potential and spherical structure (Fig. S8), revealing their robust photothermal stability. Similarly, for PDA nanoparticles suffered from three cycles of continuous NIR laser irradiation, their NIR-

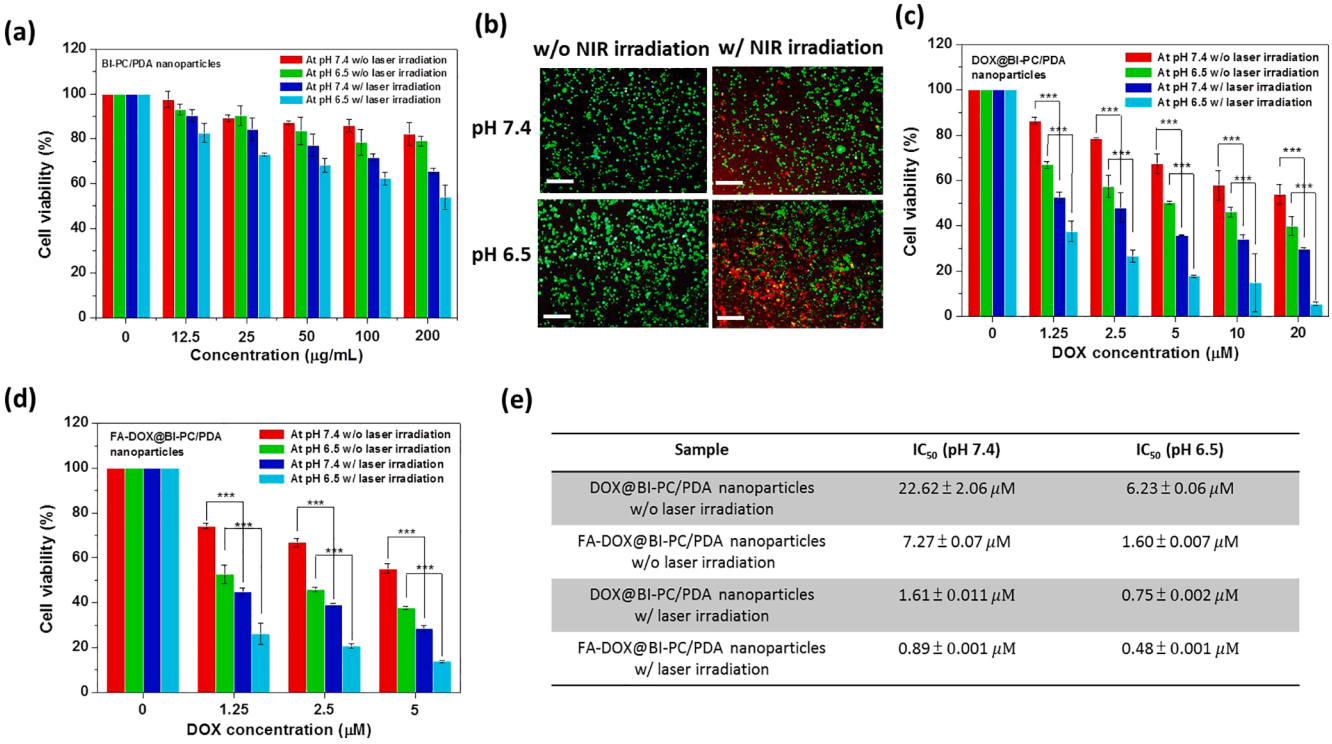

(e)

Sample	IC_{50} (pH 7.4)	IC_{50} (pH 6.5)
DOX@BI-PC/PDA nanoparticles w/o laser irradiation	22.62 ± 2.06 μM	6.23 ± 0.06 μM
FA-DOX@BI-PC/PDA nanoparticles w/o laser irradiation	7.27 ± 0.07 μM	1.60 ± 0.007 μM
DOX@BI-PC/PDA nanoparticles w/ laser irradiation	1.61 ± 0.011 μM	0.75 ± 0.002 μM
FA-DOX@BI-PC/PDA nanoparticles w/ laser irradiation	0.89 ± 0.001 μM	0.48 ± 0.001 μM

Fig. 6. (a) Viability of CT-26 cells incubated with BI-PC/PDA nanoparticles at pH 7.4 and 6.5 for 24 h with and without the 5-min NIR laser irradiation (1.25 W/cm^2), followed by additional 12 h incubation. (b) Fluorescence images of CT-26 cells treated with BI-PC/PDA nanoparticles (200 μg/mL) at pH 7.4 and 6.5 for 24 h with and without the 5-min NIR laser irradiation. The viable cells were stained green with Calcein AM, and the dead cells were stained red with PI. Scale bars are 100 μm. Viability of CT-26 cells incubated with (c) DOX@BI-PC/PDA nanoparticles and (d) FA-DOX@BI-PC/PDA nanoparticles at pH 7.4 and 6.5, respectively, in the absence or presence of NIR laser irradiation. (e) IC_{50} values of different treatments on CT-26 cells.

triggered hyperthermia capability was nearly unvaried (Fig. S9).

3.4. Characterization and acidity/NIR-responsive drug release of DOX@BI-PC/PDA nanoparticles

Through the hydrophobic and π-π stacking interactions between DOX and PDA, DOX was efficiently incorporated into the BI-PC/PDA nanoparticles (Scheme 2b). As shown in the UV/Vis spectrum of DOX@BI-PC/PDA nanoparticles (Fig. 2a), the feature absorption peak of DOX at 480 nm was observed, confirming the successful DOX encapsulation. After being loaded with DOX molecules, the particle size of BI-PC/PDA nanoparticles was slightly enlarged from 146.6 nm to 158.8 nm (Fig. 2f and Table 1). The drug loading efficiency and content of DOX@BI-PC/PDA nanoparticles were determined to be ca. 88.1 % and 15.0 wt%, respectively. It should be mentioned that the DOX@BI-PC/PDA nanoparticles still exhibited well-dispersed spherical shape and outstanding colloidal stability in serum-containing PBS (Fig. 3d, f and h), being similar to BI-PC/PDA nanoparticles. Note that the DOX@BI-PC/PDA nanoparticles also displayed structural swollen and surface charge conversion in response to pH reduction from 7.4 to 5.0 by the acidity-triggered protonation of chitosan and dePEGylation, as reflected by the increased R_g/R_h ratio and zeta potential (Fig. S10 and 3i). This is particular important that the DOX@BI-PC/PDA nanoparticles showed slightly positively-charged surfaces owing to PEG detachment and chitosan protonation when exposed to the weak acidic environment (pH 6.5) close to pH_e, a key factor for the promoted cellular uptake by cancer cells within acidic tumor microenvironment. As presented in Fig. 5a, for DOX@BI-PC/PDA nanoparticles, the cumulative drug release over 24 h was appreciably promoted from 31.2 to 53.5 % as the solution pH being changed from 7.4 to 4.0. This could be attributed to the following reasons. First, the enhanced protonation of DOX payloads in acidic environment partly declined their hydrophobic and π-π stacking interactions with hybrid nanoparticles. Second, the acidity-induced swelling, chitosan protonation and PEG detachment of DOX@BI-PC/PDA nanoparticles probably accelerated DOX outflow. Furthermore, the drug liberation from DOX@BI-PC/PDA nanoparticles was further promoted by 808 nm NIR laser irradiation because the π-π stacking and hydrophobic interactions between DOX molecules and hybrid nanoparticles were partially diminished by the photo-triggered hyperthermia. Similar findings regarding the acidity/thermal-triggered rapid DOX release from various PDA-based nanoparticles were also reported elsewhere [11,50,51]. Presumably, the DOX@BI-PC/PDA nanoparticles could achieve the acidity/thermal-responsive rapid DOX liberation at acidic endosome/lysosome under an externally remote-controlled NIR irradiation stimuli, thus decreasing the side effect of anticancer drugs and boosting antitumor effect.

3.5. In vitro tumor acidity/FA receptor-mediated cellular uptake

To endow the DOX@BI-PC/PDA nanoparticles with ability capable of actively targeting FA receptor overexpressed cancer cells, FA molecules were covalently modified on the surfaces of DOX@BI-PC/PDA nanoparticles upon Michael addition reaction between FA and PDA (Scheme 2b). An appreciably increased peak intensity of C = O (531.0 eV) and C-O (532.5 eV) was observed in the XPS spectrum of FA-BI-PC/PDA nanoparticles (Fig. 2d), confirming the successful modification of FA ligands on the surfaces of hybrid nanoparticles. In addition to drug loading content, the particle size and zeta potential of FA-DOX@BI-PC/PDA nanoparticles in aqueous solutions were comparable to those of DOX@BI-PC/PDA nanoparticles (Table 1, Fig. 2f and 3i). Also, the FA-DOX@BI-PC/PDA nanoparticles suspended in pH 7.4 aqueous solutions at 37 °C for 24 h retained nearly unvaried zeta potential and well-dispersed spherical shape, being similar to the BI-PC/PDA and DOX@BI-PC/PDA nanoparticles (Fig. S11). Notably, the virtually unchanged

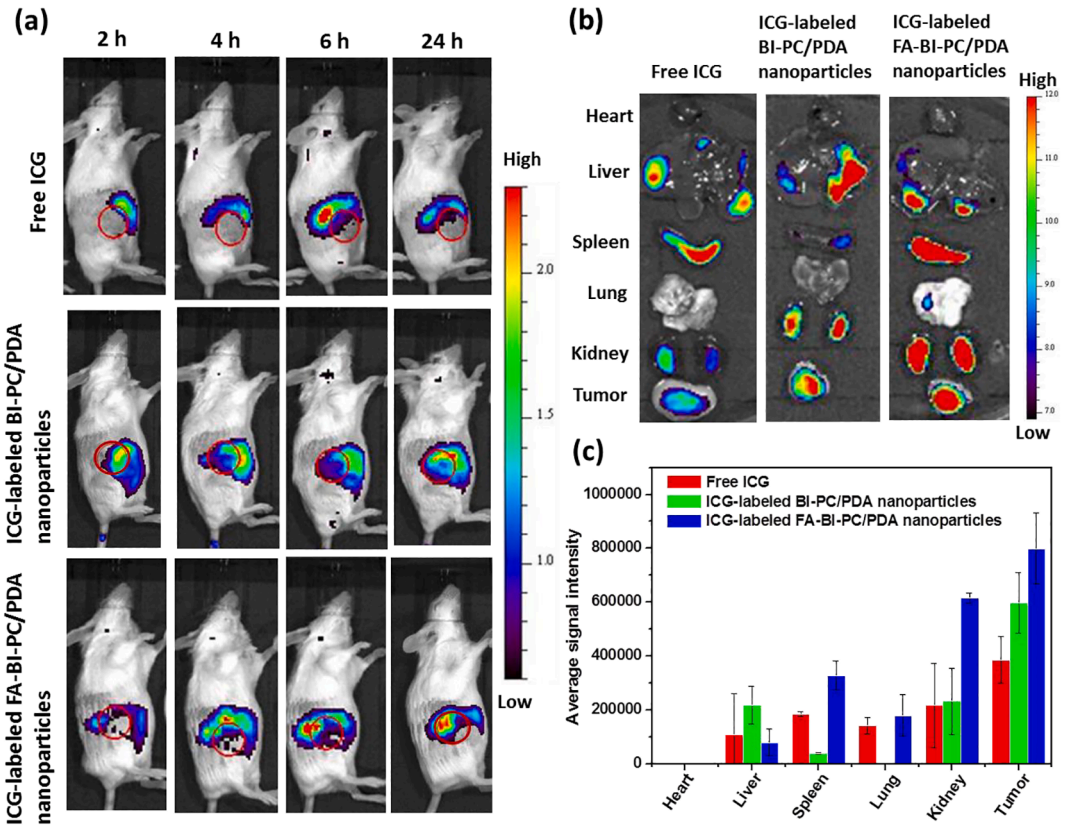

Fig. 7. (a) In vivo NIR fluorescence images of CT-26 tumor-bearing mice receiving intravenous injection of different ICG-containing formulations attained by IVIS. The tumor sites were highlighted with red circle. (b) NIR fluorescence images of the isolated major organs and tumors at 48 h post-injection with different ICG-containing formulations. (c) Average ICG fluorescence intensities of individual organs and tumor from CT-26 tumor-bearing mice treated with different ICG-containing formulations (n = 4 per group).

particle size of FA-DOX@BI-PC/PDA nanoparticles in 10 % FBS-containing PBS at 37 °C for 24 h was also attained (Fig. S12). These findings suggest the prominent colloidal stability of FA-DOX@BI-PC/PDA nanoparticles in aqueous phase, being beneficial to their in vivo tumor-targeted DOX delivery.

The effects of pH_e-triggered PEG detachment and FA exposure of FA-DOX@BI-PC/PDA nanoparticles on the cellular uptake were investigated using FA receptor-overexpressed mouse colon carcinoma cell, CT-26, as a cell model. As presented in the CLSM images (Fig. 5b), with 4-h incubation, DOX transported by DOX@BI-PC/PDA nanoparticles at pH 6.5 was found appreciably in the cytoplasm of CT-26 cells, whereas quite small amounts of DOX delivered by the counterparts at pH 7.4 were observed intracellularly. Also, the flow cytometric histograms showed that the DOX fluorescence intensity of CT-26 cells incubated with DOX@BI-PC/PDA nanoparticles for 4 h was ca. 1.4-fold enhanced in response to the culture pH reduction from 7.4 to 6.5 (Fig. 5c and d). Such an acidity-induced increase in the cellular uptake of DOX@BI-PC/PDA nanoparticles was obtained with another cell model, TRAMP-C1 cancer cells (Fig. S13). These findings strongly suggest that the cellular uptake of DOX@BI-PC/PDA nanoparticles under weak acidic condition could be boosted by their increased affinity for cancer cells upon dePEGylation. More importantly, the DOX fluorescence intensity of CT-26 cells treated with FA-DOX@BI-PC/PDA nanoparticles at pH 6.5 for 4 h was further enhanced compared with that of cancer cells incubated with DOX@BI-PC/PDA nanoparticles at the same pH (Fig. 5b, c and d). Note that the internalization of FA-DOX@BI-PC/PDA nanoparticles by CT-26 cells at pH 6.5 in the presence of free FA molecules was partly inhibited, as reflected by the reduced DOX fluorescence of CT-26 cells (Fig. 5b). These results convincingly demonstrate that the dePEGylation and FA exposure of FA-DOX@BI-PC/PDA nanoparticles in weak acidic milieu mimicking tumor extracellular acidity could prominently increase their affinity for CT-26 cells, thus facilitating intracellular DOX delivery upon FA receptor-mediated endocytosis (Scheme 1). However, the cellular uptake of free DOX by CT-26 and TRAMP-C1 cells was considerably higher than that of DOX@BI-PC/PDA nanoparticles with and without FA ligand decoration (Fig. 5b and S13). This could be attributed to the different routes of cellular internalization for free DOX molecules (passive diffusion) and hybrid nanoparticles (endocytosis) [52,53].

3.6. *In vitro photothermal/chemo combination therapy*

Encouraged by the excellent NIR-triggered hyperthermia capability of BI-PC/PDA nanoparticles, we evaluated their PTT-mediated anticancer potency on CT-26 cells. As an essential control, in the lack of NIR laser irradiation, CT-26 cells incubated with BI-PC/PDA nanoparticles (12.5 ~ 200 μg/mL) at pH 7.4 and 6.5 for 24 h maintained the viability beyond 80 % (Fig. 6a), suggesting the negligible toxicity of hybrid nanoparticles to cancer cells. Note that, after 5-min NIR laser irradiation, the viability of CT-26 cells incubated with BI-PC/PDA nanoparticles at pH 6.5 for 24 h was appreciably reduced in hybrid nanoparticle concentration-dependent manner compared to that of CT-26 cells treated with the counterparts at pH 7.4 for 24 h. Also, as revealed in the fluorescence staining of live/dead CT-26 cells (Fig. 6b), with 5-min NIR laser irradiation, most of CT-26 cells treated with BI-PC/PDA nanoparticles (200 μg/mL) at pH 6.5 showed remarkable PI-positive staining relative to cells incubated with the counterparts at pH 7.4. The data suggest that the anticancer efficacy of PTT delivered by BI-PC/PDA nanoparticles could be enhanced by means of the promoted cellular uptake upon acidity-activated PEG detachment. On the other

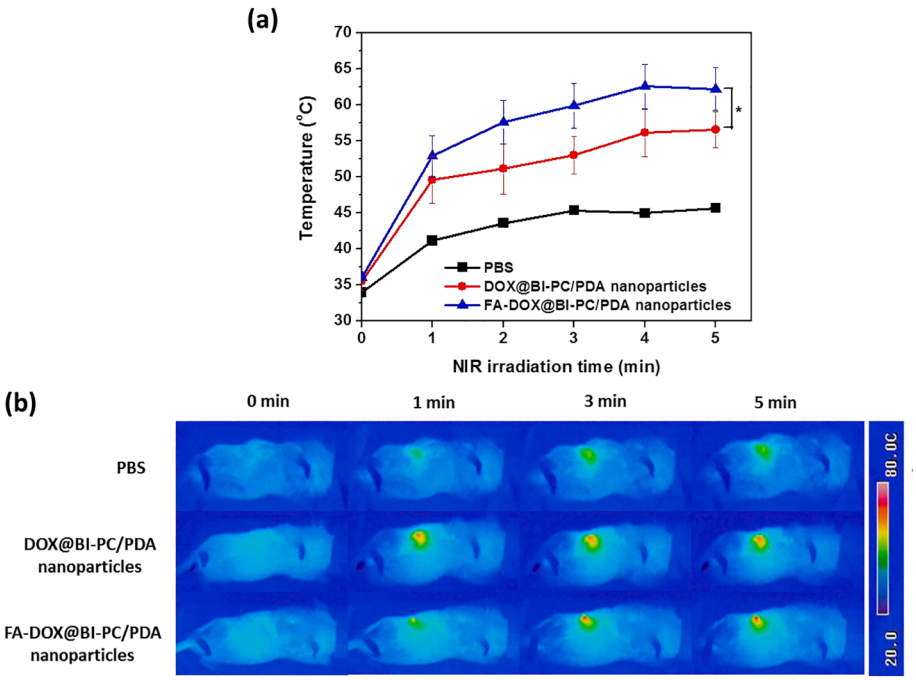

Fig. 8. (a) Temperature profiles and (b) infrared thermographic maps at the tumor sites of CT-26 tumor-bearing mice receiving DOX@BI-PC/PDA or FA-DOX@BI-PC/PDA nanoparticles and exposed to 5-min 808 nm NIR laser irradiation of 1.25 W/cm^2 at 6 h post-injection.

hand, with and without NIR laser irradiation, free DOX molecules showed similar cytotoxicity in inhibiting the proliferation of CT-26 cells (Fig. S14), signifying that the presence of laser irradiation had few influences on DOX-mediated anticancer potency. Note that, in the absence of NIR laser irradiation, the viability of CT-26 cells incubated with DOX@BI-PC/PDA nanoparticles for 24 h was considerably decreased in DOX concentration-dependent manner, in particular with the pH of culture medium being adjusted from 7.4 to 6.5 (Fig. 6c). Also, the drug doses required for 50 % cellular growth inhibition (IC_{50}) value of DOX@BI-PC/PDA nanoparticles at pH 6.5 attained to be ca. 6.23 μM is significantly 3.6-fold lower than that (22.62 μM) of the counterparts at pH 7.4 (Fig. 6e). Similar findings were also attained with TRAMP-C1 cancer cells (Fig. S15). Such a pH-dependent cytotoxicity demonstrates again that the DOX@BI-PC/PDA nanoparticles effectively augment DOX chemotherapy efficacy upon the increased cellular uptake and intracellular DOX transport driven by acidity-triggered dePEGylation as revealed in Fig. 5b, c and d. Compared to the DOX@BI-PC/PDA nanoparticles, the FA-DOX@BI-PC/PDA nanoparticles remarkably lowered IC_{50} on CT-26 cells, in particular incubation with cancer cells at pH 6.5 (Fig. 6d and e). However, for TRAMP-C1 cells with low expression of FA receptors, the DOX@BI-PC/PDA nanoparticles with and without FA decoration exhibited similar IC_{50} values in the lack of NIR laser irradiation (Fig. S15). Evidently, the acidity-elicited dePEGylation and FA targeting of FA-DOX@BI-PC/PDA nanoparticles play a key role in enhancing their anticancer efficacy on the FA receptor-overexpressed cancer cells. More importantly, with NIR laser irradiation, the FA-DOX@BI-PC/PDA nanoparticles at very low DOX concentrations (1.25 and 2.5 μM) incubated with CT-26 cells at pH 6.5 exhibited the powerful capability in suppressing the proliferation of cancer cells by combined photothermal/chemo therapy (Fig. 6d and e). Based on the above results, it can be concluded that the designed FA-DOX@BI-PC/PDA nanoparticles could realize a low drug dosage but effective anticancer activity against CT-26 cells, mainly due to the boosted cellular uptake upon acidity-activated PEG detachment and FA receptor-mediated endocytosis, NIR-triggered intracellular DOX release and PDA-mediated PTT.

3.7. *In vivo tumor accumulation and biodistribution analysis*

As shown above, the uptake of FA-DOX@BI-PC/PDA nanoparticles by both CT-26 and TRAMP-C1 cells was remarkably promoted in response to the in vitro imitated weak acidic tumor microenvironments. Next, we investigated the effects of the pH_e-responsive dePEGylation and FA targeting of FA-BI-PC/PDA nanoparticles on in vivo tumor accumulation and biodistribution using the subcutaneous CT-26 tumor model in female BALB/c mice. For comparison, BI-PC/PDA nanoparticles which lacked FA decoration were employed in this work. Considering the poor NIR fluorescence property of DOX and unneglectable auto-fluorescence of BALB/c mice, the FA-BI-PC/PDA and BI-PC/PDA nanoparticles were labeled with amphiphilic ICG, a NIR dye, for observation of fluorescence imaging. Upon intravenous injections with various ICG-labeled hybrid nanoparticles, the tumor accumulation of hybrid nanoparticles within tumor-bearing mice was monitored by vivo ICG fluorescence imaging. In comparison with the weak fluorescence signals in the tumor sites of free ICG group at 6 and 24 h post-injection, the profound fluorescence signals in tumor regions of ICG-labeled hybrid nanoparticle groups during the identical time period were detected (Fig. 7a). This proves the pronounced ability of ICG-labeled hybrid nanoparticle in enhancing their accumulation in tumor sites through the EPR effect. It is worth to note that the ICG fluorescence intensities at the tumor sites of ICG-labeled FA-BI-PC/PDA nanoparticle group were appreciably higher than that of ICG-labeled BI-PC/PDA nanoparticles group over the time course. Moreover, compared to weak ex vivo NIR fluorescence signals of tumor receiving free ICG at 48 h post-injection, the fluorescence intensity of tumors from ICG-labeled hybrid nanoparticle groups was appreciably higher, in particular for ICG-labeled FA-BI-PC/PDA nanoparticles (Fig. 7b and c). These findings clearly illustrate that the PEG detachment and active FA tumor targeting of ICG-labeled FA-BI-PC/PDA nanoparticles deposited within tumor extracellular acidity could largely promote their internalization by CT-26 cells upon FA-receptor mediated endocytosis, thereby augmenting their accumulation in tumor to prevent ICG from body clearance and degradation by liver. By contrast, owing to the lack of FA decoration, the tumor accumulation of ICG-labeled BI-PC/PDA nanoparticles was not prominent.

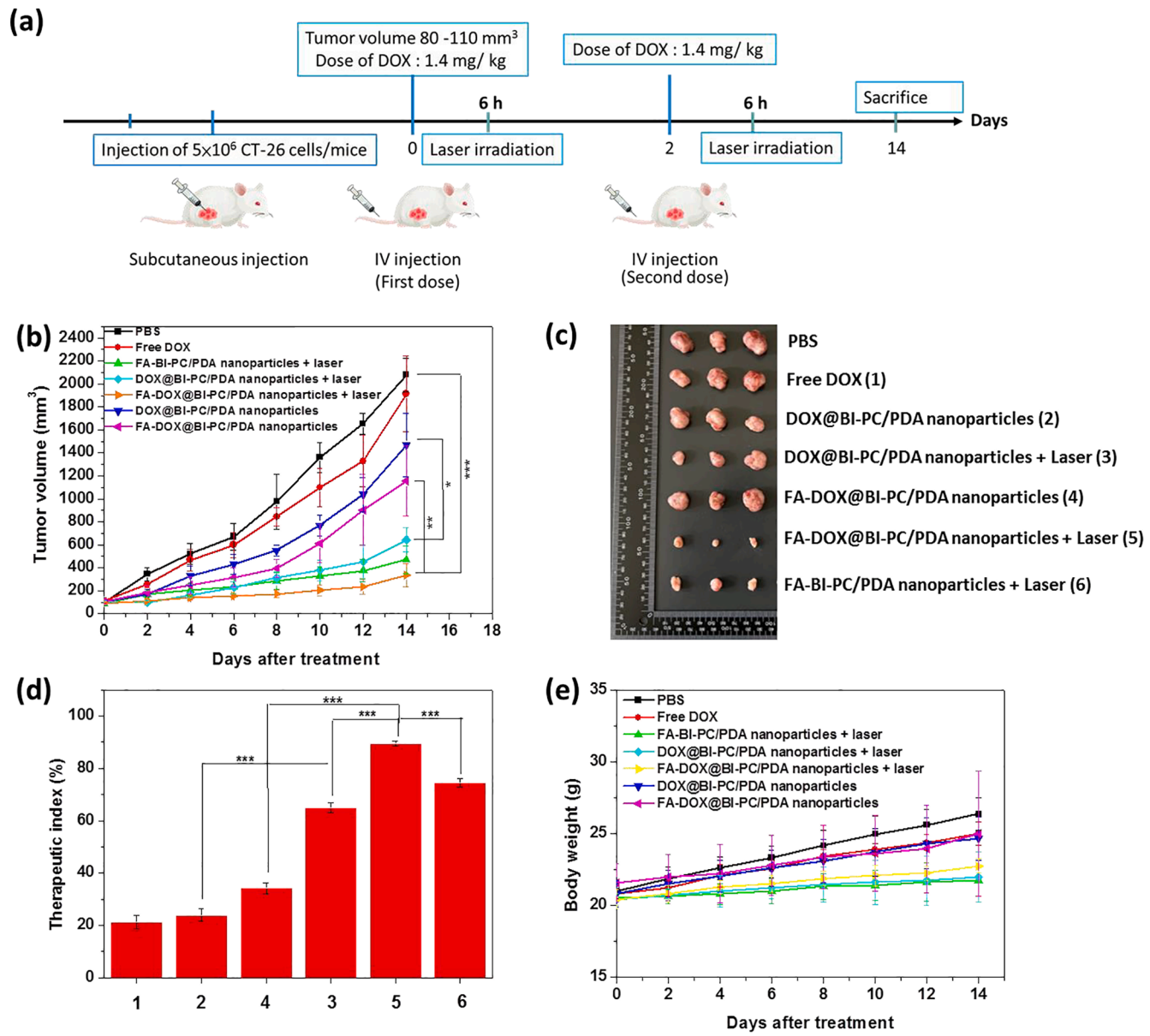

Fig. 9. (a) Experimental flowchart of in vivo tumor growth inhibition study. (b) Tumor growth inhibition profiles of CT-26 tumor-bearing mice injected with various formulations, followed by NIR laser irradiation (5 min, 1.25 W/cm^2) at 6 h post-injection or without any laser treatment. (c) Morphology and size of the tumors isolated from the euthanized mice at day 14 (the end point) after the treatment. (d) TI value of different treatments. (e) Body weight of CT-26 tumor-bearing receiving different treatments with and without 808 nm NIR irradiation.

3.8. In vivo tumor growth inhibition by photothermal/chemo combinatorial therapy

As presented in Fig. 8, a considerable elevation in local tumor temperature during NIR laser irradiation (1.25 W/cm^2) at 6 h post-injection of PDA-containing hybrid nanoparticles was observed, indicating the effective NIR-triggered hyperthermia on tumor. Notably, compared to DOX@BI-PC/PDA nanoparticles, the FA-DOX@BI-PC/PDA nanoparticles caused relatively intense NIR-activated hyperthermia on tumor where a temperature as high as 62.6 °C was gained, due to their substantial deposition in tumor site as revealed in Fig. 7. Moreover, as presented in Fig. S16, the formation of burning scar at the irradiated tumor sites at day 14 post-treatment reveals that the hyperthermia beyond 50 °C can readily led to irreversible injury to cancer cells.

The in vivo antitumor potencies of various formulations in terms of the change of tumor volume of CT-26 tumor-bearing mice were explored for up to 14 days post first intravenous injection (Fig. 9a and b). After 14 days post treatment, a significant enlargement in the tumor volume of mice treated with free DOX was observed (Fig. 9b), indicating the failure of tumor growth inhibition because of poor tumor accumulation of DOX molecules and nature chemotherapy resistance of CT- 26 tumor [54]. By contrast, the administration of FA-DOX@BI-PC/PDA and DOX@BI-PC/PDA nanoparticles without laser irradiation induced a limited inhibition on tumor growth over the time period of 8 days post injection, beyond which tumors receiving the above formulations progressively enlarged. This indicates that the tumor-targeted single DOX chemotherapy delivered by the hybrid nanoparticles upon EPR effect cannot efficiently suppress tumor growth. Note that the single PTT transport by FA-BI-PC/PDA nanoparticles considerably retarded tumor growth as compared to the single chemotherapy delivered by the aforementioned two DOX-loaded formulations, indicating the effective antitumor efficacy of tumor-targeted PTT. More importantly, by virtue of the NIR-activated hyperthermia combined with DOX chemotherapy, the FA-DOX@BI-PC/PDA nanoparticles potently inhibited tumor growth in

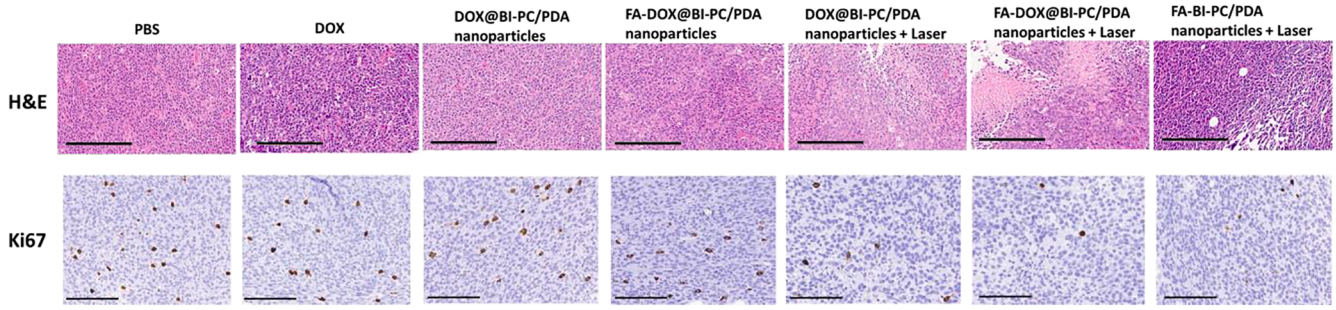

Fig. 10. Representative images of tumor sections with H&E and Ki67 staining from CT-26 tumor-bearing mice receiving different treatments. Scale bars are 200 μm.

comparison with single PTT or chemotherapy. The findings suggest that the photo-elicited hyperthermia of FA-DOX@BI-PC/PDA nanoparticles accumulated within tumor sites not only leads to considerable thermal ablation of cancer cells but also promotes intracellular DOX release, thereby largely hindering cancer cell proliferation. On the other hand, under dual-modality therapy, the FA-DOX@BI-PC/PDA nanoparticles exhibited antitumor potency superior to DOX@BI-PC/PDA nanoparticles. This is primarily attributed to that the tumor acidity-triggered PEG detachment and active FA targeting of FA-DOX@BI-PC/PDA nanoparticles prominently facilitate their cellular uptake and tumor accumulation (Fig. 5b, c and d, and Fig. 7), thus maximizing the antitumor efficacy of photothermal/chemo therapy. Being corresponding to the data of in vivo tumor growth inhibition, tumors collected from the euthanized mice receiving FA-DOX@BI-PC/PDA nanoparticles and NIR irradiation were the smallest among the tumors with other treatments (Fig. 9c).

To quantify antitumor therapeutic efficacy, the TI was obtained based on the following equation. TI (%) = (1-(weight of tumor in the experimental group)/(weight of tumor in the PBS group)) × 100%. As shown in Fig. 9d, the average TI (ca 89.4 %) of FA-DOX@BI-PC/PDA nanoparticles plus NIR irradiation is significantly higher than that (34.2 %) of the counterparts without NIR irradiation, that (74.7 %) of FA@BI-PC/PDA nanoparticles plus NIR irradiation and that (65.0 %) of DOX@BI-PC/PDA nanoparticles with NIR illumination. These data prove again that the dual-modality therapy transported by FA-DOX@BI-PC/PDA nanoparticles has the best antitumor ability. Furthermore, no significant change in body weight of the treated mice over time in all groups was observed, illustrating that these formulations employed in this study did not elicit severe acute toxicity (Fig. 9e).

In the H&E staining images of the tumor sections (Fig. 10), for CT-26 tumor receiving PBS as the control, most of the cancer cells retained their normal morphology, whereas the tumor cells were partly destroyed and became necrotic for single chemotherapy-treated groups. Upon laser irradiation, tumors treated with FA-DOX@BI-PC/PDA nanoparticles exhibited more extensive apoptosis and necrosis in comparison with those treated with either DOX@BI-PC/PDA nanoparticles or FA-BI-PC/PDA nanoparticles. Also, a considerable decrease in the expression level of Ki67, a proliferation marker, was attained in the tumor sections from FA-DOX@BI-PC/PDA nanoparticle group with NIR laser irradiation as compared to other groups, signifying strong anti-proliferative effects of tumor-targeted photothermal/chemo therapy on xenograft tumors. These results strongly demonstrate the maximized antitumor effect of the photothermal/chemo therapy delivered by FA-DOX@BI-PC/PDA nanoparticles via effective tumor uptake driven by tumor acidity-triggered PEG detachment and active FA-mediated tumor targeting. Also, due to selectively NIR-activated hyperthermia of tumor sites, no considerable damage was observed in major organs of mice treated with all nanoformulations (Fig. S17). Even though the encouraging in vivo results were attained in this study, there are still some hurdles for the clinical applications of cancer PTT. Indeed, for several kinds of cancers, such as skin and oral cancers, selective and effective NIR irradiation at tumor tissues can be conducted with the aid of optical fibers, thus obtaining satisfied antitumor efficacy [55,56]. However, the therapeutic potency of PTT was significantly lowered for some other deeply located tumors. To enhance the antitumor performance of PTT, the easy-to-use medical apparatus that can deliver light into deep tissues should be extensively developed.

4. Conclusions

To considerably boost antitumor efficacy of the combined photothermal/chemo therapy, the tumor acidity-responsive FA-BI-PC/PDA nanoparticles were developed to deliver DOX to tumor in a more selective and efficient manner. The FA-DOX@BI-PC/PDA nanoparticles not only showed prominent colloidal stability in serum-containing environment and photothermal conversion efficiency, but also exhibited acidity/photothermal-activated drug release. The in vitro cellular uptake findings showed that the cellular uptake of FA-DOX@BI-PC/PDA nanoparticles by FA receptor-overexpressed CT-26 cancer cells under weak acidic conditions was greatly enhanced upon their dePEGylation and active FA targeting. The in vivo studies further illustrate that the FA-DOX@BI-PC/PDA nanoparticles not only efficiently accumulate within CT-26 solid tumor but also generate effective hyperthermia on tumor by virtue of NIR laser irradiation. Through the potent photothermal effects combined with DOX chemotherapy, the FA-DOX@BI-PC/PDA nanoparticles considerably inhibited tumor growth without significant side effect. Over all, the FA-DOX@BI-PC/PDA nanoparticles featured with an effective tumor accumulation, cellular uptake and photothermal/chemo dual-modality therapy exhibit great potential in enhancing cancer treatment.

Declaration of Competing Interest

The authors declare that they have no known competing financial interests or personal relationships that could have appeared to influence the work reported in this paper.

Acknowledgements

This work is supported by the Ministry of Science and Technology (MOST 108-2221-E-005- 024-MY2, MOST 110-2628-E-005-001, MOST110-2731-M-005-001), National Chung Hsing University and Chung Shan Medical University (NCHU-CSMU 11003), Taiwan.

Appendix A. Supplementary data

Supplementary data to this article can be found online at https://doi.org/10.1016/j.cej.2022.137243.

References

[1] J. Shi, P.W. Kantoff, R. Wooster, O.C. Farokhzad, Cancer nanomedicine: progress, challenges and opportunities, Nat. Rev. Cancer 17 (1) (2017) 20–37.
[2] Y. Dang, J. Guan, Nanoparticle-based drug delivery systems for cancer therapy, Smart Materials in Medicine 1 (2020) 10–19.

[3] S. Senapati, A.K. Mahanta, S. Kumar, P. Maiti, Controlled drug delivery vehicles for cancer treatment and their performance, Sig Transduct Target Ther 3 (2018) 7.

[4] Q. Song, Y. Yin, L. Shang, T. Wu, D. Zhang, M. Kong, Y. Zhao, Y. He, S. Tan, Y. Guo, Z. Zhang, Tumor microenvironment responsive nanogel for the combinatorial antitumor effect of chemotherapy and immunotherapy, Nano Lett. 17 (10) (2017) 6366–6375.

[5] X.u. Li, S.A. Valdes, R.F. Alzhrani, S. Hufnagel, S.D. Hursting, Z. Cui, Zoledronic acid-containing nanoparticles with minimum premature release show enhanced activity against extraskeletal tumor, ACS Appl. Mater. Interfaces 11 (7) (2019) 7311–7319.

[6] J. Li, P. Liu, One-pot fabrication of pH/reduction dual-stimuli responsive chitosan-based supramolecular nanogels for leakage-free tumor-specific DOX delivery with enhanced anti-cancer efficacy, Carbohydr. Polym. 201 (2018) 583–590.

[7] V. Jain, S. Jain, S.C. Mahajan, Nanomedicines based drug delivery systems for anti-cancer targeting and treatment, Curr. Drug Deliv. 12 (2015) 177–191.

[8] C. Holohan, S. Van Schaeybroeck, D.B. Longley, P.G. Johnston, Cancer drug resistance: an evolving paradigm, Nat. Rev. Cancer 13 (10) (2013) 714–726.

[9] Y. Xing, T. Ding, Z. Wang, L. Wang, H. Guan, J. Tang, D. Mo, J. Zhang, Temporally controlled photothermal/photodynamic and combined therapy for overcoming multidrug resistance of cancer by polydopamine nanoclustered micelles, ACS Appl. Mater. Interfaces 11 (15) (2019) 13945–13953.

[10] Y. Bao, M. Yin, X. Hu, X. Zhuang, Y. Sun, Y. Guo, S. Tan, Z. Zhang, A safe, simple and efficient doxorubicin prodrug hybrid micelle for overcoming tumor multidrug resistance and targeting delivery, J. Control. Release 235 (2016) 182–194.

[11] S. Liu, J. Pan, J. Liu, Y. Ma, F. Qiu, L. Mei, X. Zeng, G. Pan, Dynamically PEGylated and borate-coordination-polymer-coated polydopamine nanoparticles for synergetic tumor-Targeted, chemo-photothermal combination therapy, Small 14 (2018) 1703968.

[12] C.-C. Hung, W.-C. Huang, Y.-W. Lin, T.-W. Yu, H.-H. Chen, S.-C. Lin, W.-H. Chiang, H.-C. Chiu, Active tumor permeation and uptake of surface charge-switchable theranostic nanoparticles for imaging-guided photothermal/chemo combinatorial therapy, Theranostics 6 (3) (2016) 302–317.

[13] J. Feng, Z. Xu, P. Dong, W. Yu, F. Liu, Q. Jiang, F. Wang, X. Liu, Stimuli-responsive multifunctional metal-organic framework nanoparticles for enhanced chemo-photothermal therapy, J. Mater. Chem. B 7 (6) (2019) 994–1004.

[14] H. He, E. Markoutsa, Y. Zhan, J. Zhang, P. Xu, Mussel-inspired PLGA/polydopamine core-shell nanoparticle for light induced cancer thermochemotherapy, Acta Biomater. 59 (2017) 181–191.

[15] Z. Li, M. Wu, H. Bai, X. Liu, G. Tang, Light-enhanced hypoxia-responsive nanoparticles for deep tumor penetration and combined chemo-photodynamic therapy, Chem. Commun. 54 (93) (2018) 13127–13130.

[16] X. Wei, L. Liu, X. Li, Y. Wang, X. Guo, J. Zhao, S. Zhou, Selectively targeting tumor-associated macrophages and tumor cells with polymeric micelles for enhanced cancer chemo-immunotherapy, J. Control. Release 313 (2019) 42.

[17] Z. Ren, S. Sun, R. Sun, G. Cui, L. Hong, B. Rao, A. Li, Z. Yu, Q. Kan, Z. Mao, A metal-polyphenol-coordinated nanomedicine for synergistic cascade cancer chemotherapy and chemodynamic therapy, Adv. Mater. 32 (2020) 1906024.

[18] Y.-T. Liao, C.-H. Liu, Y. Chin, S.-Y. Chen, S.H. Liu, Y.-C. Hsu, K.-W. Wu, Biocompatible and multifunctional gold nanorods for effective photothermal therapy of oral squamous cell carcinoma, J. Mater. Chem. B 7 (28) (2019) 4451–4460.

[19] W. Tao, X. Ji, X. Xu, M. Ariful Islam, Z. Li, S. Chen, P.E. Saw, H. Zhang, Z. Bharwani, Z. Guo, J. Shi, O. Farokhzad, Antimonene quantum dots: synthesis and application as near-infrared photothermal agents for effective cancer therapy, Angew. Chem. Int. Ed. 56 (2017) 11896–11900.

[20] Y. Liu, Q. Guo, X. Zhu, W. Feng, L. Wang, L. Ma, G. Zhang, J. Zhou, F. Li, Optimization of Prussian blue coated NaDyF4:x%Lu nanocomposites for multifunctional imaging-guided photothermal therapy, Adv. Funct. Mater. 26 (2016) 5120–5130.

[21] X. Song, H. Gong, S. Yin, L. Cheng, C. Wang, Z. Li, Y. Li, X. Wang, G. Liu, Z. Liu, Ultra-small iron oxide doped polypyrrole nanoparticles for in vivo multimodal imaging guided photothermal therapy, Adv. Funct. Mater. 24 (9) (2014) 1194–1201.

[22] W. Tao, X. Zhu, X. Yu, X. Zeng, Q. Xiao, X. Zhang, X. Ji, X. Wang, J. Shi, H. Zhang, L. Mei, Black phosphorus nanosheets as a robust delivery platform for cancer theranostics, Adv. Mater. 29 (2017) 1603276.

[23] Y.W. Chen, Y.L. Su, S.H. Hu, S.Y. Chen, Functionalized graphene nanocomposites for enhancing photothermal therapy in tumor treatment, Adv. Drug Deliv. Rev. 105 (2016) 190–204.

[24] Y. Liu, K. Ai, L. Lu, Polydopamine and its derivative materials: synthesis and promising applications in energy, environmental, and biomedical fields, Chem. Rev. 114 (2014) 5057–5115.

[25] B. Poinard, S.Z.Y. Neo, E.L.L. Yeo, H.P.S. Heng, K.G. Neoh, J.C.Y. Kah, Polydopamine nanoparticles enhance drug release for combined photodynamic and photothermal therapy, ACS Appl. Mater. Interfaces 10 (25) (2018) 21125–21136.

[26] H. Lee, S.M. Dellatore, W.M. Miller, P.B. Messersmith, Mussel-inspired surface chemistry for multifunctional coatings, Science 318 (5849) (2007) 426–430.

[27] H. Wu, H. Hu, J. Wan, Y. Li, Y. Wu, Y. Tang, C. Xiao, H. Xu, X. Yang, Z. Li, Hydroxyethyl starch stabilized polydopamine nanoparticles for cancer chemotherapy, Chem. Eng. J. 349 (2018) 129–145.

[28] X. Yu, X. Tang, J. He, X. Yi, G. Xu, L. Tian, R. Zhou, C. Zhang, K. Yang, Polydopamine nanoparticle as a multifunctional nanocarrier for combined radiophotodynamic therapy of cancer, Part. Part. Syst. Char. 34 (2017) 1600296.

[29] V.P. Torchilin, Multifunctional, stimuli-sensitive nanoparticulate systems for drug delivery, Nat. Rev. Drug Discov. 13 (11) (2014) 813–827.

[30] H.Y. Yang, M.-S. Jang, G.H. Gao, J.H. Lee, D.S. Lee, Construction of redox/pH dual stimuli-responsive PEGylated polymeric micelles for intracellular doxorubicin delivery in liver cancer, Polym. Chem. 7 (9) (2016) 1813–1825.

[31] J.M. Harris, R.B. Chess, Effect of pegylation on pharmaceuticals, Nat. Rev. Drug Discovery 2 (3) (2003) 214–221.

[32] F.M. Veronese, G. Pasut, PEGylation, successful approach to drug delivery, Drug Discovery Today 10 (21) (2005) 1451–1458.

[33] N. Guo, Y.i. Zhou, T. Wang, M. Lin, J. Chen, Z. Zhang, X. Zhong, Y. Lu, Q. Yang, D. Xu, J. Gao, M. Han, Specifically eliminating tumor-associated macrophages with an extra- and intracellular stepwise-responsive nanocarrier for inhibiting metastasis, ACS Appl. Mater. Interfaces 12 (52) (2020) 57798–57809.

[34] Z. Yang, N. Sun, R. Cheng, C. Zhao, Z. Liu, X. Li, J. Liu, Z. Tian, pH multistage responsive micellar system with charge-switch and PEG layer detachment for co-delivery of paclitaxel and curcumin to synergistically eliminate breast cancer stem cells, Biomaterials 147 (2017) 53–67.

[35] X. Zeng, G. Liu, W. Tao, Y. Ma, X. Zhang, F. He, J. Pan, L. Mei, G. Pan, A drug-self-gated mesoporous antitumor nanoplatform based on pH-sensitive dynamic covalent bond, Adv. Funct. Mater. 27 (2017) 1605985.

[36] Y.N. Hung, Y.L. Liu, Y.H. Chou, S.H. Hu, B. Cheng, W.H. Chiang, Promoted cellular uptake and intracellular cargo release of ICG/DOX-carrying hybrid polymeric nanoassemblies upon acidity-activated PEG detachment to enhance cancer photothermal/chemo combination therapy, Eur. Polym. J. 163 (2022), 110944.

[37] E. Koren, A. Apte, A. Jani, V.P. Torchilin, Multifunctional PEGylated 2C5-immunoliposomes containing pH-sensitive bonds and TAT peptide for enhanced tumor cell internalization and cytotoxicity, J. Control. Release 160 (2) (2012) 264–273.

[38] L.i. Kong, F. Campbell, A. Kros, DePEGylation strategies to increase cancer nanomedicine efficacy, Nanoscale Horiz. 4 (2) (2019) 378–387.

[39] L. Zhu, P. Kate, V.P. Torchilin, Matrix metalloprotease 2-responsive multifunctional liposomal nanocarrier for enhanced tumor targeting, ACS Nano 6 (4) (2012) 3491–3498.

[40] Z. Zou, X. He, D. He, K. Wang, Z. Qing, X. Yang, L. Wen, J. Xiong, L. Li, L. Cai, Programmed packaging of mesoporous silica nanocarriers for matrix metalloprotease 2-triggered tumor targeting and release, Biomaterials 58 (2015) 35–45.

[41] G. Salzano, D.F. Costa, C. Sarisozen, E.d. Luther, G. Mattheolabakis, P. P. Dhargalkar, V.P. Torchilin, mixed nanosized polymeric micelles as promoter of doxorubicin and miRNA-34a co-delivery triggered by dual stimuli in tumor tissue, Small 12 (35) (2016) 4837–4848.

[42] X. Zang, X. Zhang, H. Hu, M. Qiao, X. Zhao, Y. Deng, D. Chen, Targeted delivery of zoledronate to tumor-associated macrophages for cancer immunotherapy, Mol. Pharm. 16 (5) (2019) 2249–2258.

[43] L.u. Zhong, L.u. Xu, Y. Liu, Q. Li, D. Zhao, Z. Li, H. Zhang, H. Zhang, Q. Kan, Y. Wang, J. Sun, Z. He, Transformative hyaluronic acid-based active targeting supramolecular nanoplatform improves long circulation and enhances cellular uptake in cancer therapy, Acta Pharm Sin B. 9 (2) (2019) 397–409.

[44] A.E. Smith, X. Xu, S.E. Kirkland-York, D.A. Savin, C.L. McCormick, "Schizophrenic" self-assembly of block copolymers synthesized via aqueous RAFT polymerization: from micelles to vesicles, Macromolecules 43 (2010) 1210–1217.

[45] D. Sprouse, Y. Jiang, J.E. Laaser, T.P. Lodge, T.M. Reineke, Tuning cationic block copolymer micelle size by pH and ionic strength, Biomacromolecules 17 (9) (2016) 2849–2859.

[46] V.T.A. Nguyen, M.-C. De Pauw-Gillet, O. Sandre, M. Gauthier, Biocompatible polyion complex micelles synthesized from arborescent polymers, Langmuir 32 (50) (2016) 13482–13492.

[47] A. Jin, Y. Wang, K. Lin, L. Jiang, Nanoparticles modified by polydopamine: Working as "drug" carriers, Bioact. Mater. 5 (3) (2020) 522–541.

[48] Y. Ni, F. Chen, L. Shi, G. Tong, J. Wang, H. Li, C. Yu, Y. Zhou, Facile preparation of water-soluble and cytocompatible small-sized chitosan-polydopamine nanoparticles, Chin. J. Chem . 35 (6) (2017) 931–937.

[49] X. Zhong, K. Yang, Z. Dong, X. Yi, Y. Wang, C. Ge, Y. Zhao, Z. Liu, Polydopamine as a biocompatible multifunctional nanocarrier for combined radioisotope therapy and chemotherapy of cancer, Adv. Funct. Mater. 25 (47) (2015) 7327–7336.

[50] W. Lei, C. Sun, T. Jiang, Y. Gao, Y. Yang, Q. Zhao, S. Wang, Polydopamine-coated mesoporous silica nanoparticles for multi-responsive drug delivery and combined chemo-photothermal therapy, Mater. Sci. Eng., C 105 (2019), 110103.

[51] Y. Lia, W. Hong, H. Zhang, T.T. Zhang, Z. Chen, S. Yuan, P. Peng, M. Xiao, L. Xu, Photothermally triggered cytosolic drug delivery of glucose functionalized polydopamine nanoparticles in response to tumor microenvironment for the GLUT1-targeting chemo-phototherapy, J. Control. Release 317 (2020) 232–245.

[52] P. Liang, D. Zhao, C.Q. Wang, J.Y. Zong, R.X. Zhuo, S.X. Cheng, Facile preparation of heparin/CaCO3/CaP hybrid nano-carriers with controllable size for anticancer drug delivery, Colloids Surf. B 102 (2013) 783–788.

[53] A. Gao, X.-l. Hu, M. Saeed, B.-F. Chen, Y.-P. Li, H.-J. Yu, Overview of recent advances in liposomal nanoparticle-based cancer immunotherapy, Acta Pharmacol. Sin. 40 (9) (2019) 1129–1137.

[54] L. Sivak, V. Subr, J. Tomala, B. Rihova, J. Strohalm, T. Etrych, M. Kovar, Overcoming multidrug resistance via simultaneous delivery of cytostatic drug and P-glycoprotein inhibitor to cancer cells by HPMA copolymer conjugate, Biomaterials 115 (2017) 65–80.

[55] D. Gao, X. Guo, X. Zhang, S. Chen, Y. Wang, T. Chen, G. Huang, Y. Gao, Z. Tian, Z. Yang, Multifunctional phototheranostic nanomedicine for cancer imaging and treatment, Mater. Today Bio 5 (2020), 100035.

[56] R. Kv, T.I. Liu, I.L. Lu, C.C. Liu, H.H. Chen, T.Y. Lu, W.H. Chiang, H.C. Chiu, Tumor microenvironment-responsive and oxygen self-sufficient oil droplet nanoparticles for enhanced photothermal/photodynamic combination therapy against hypoxic tumors, J. Control. Release 328 (2020) 87–99.